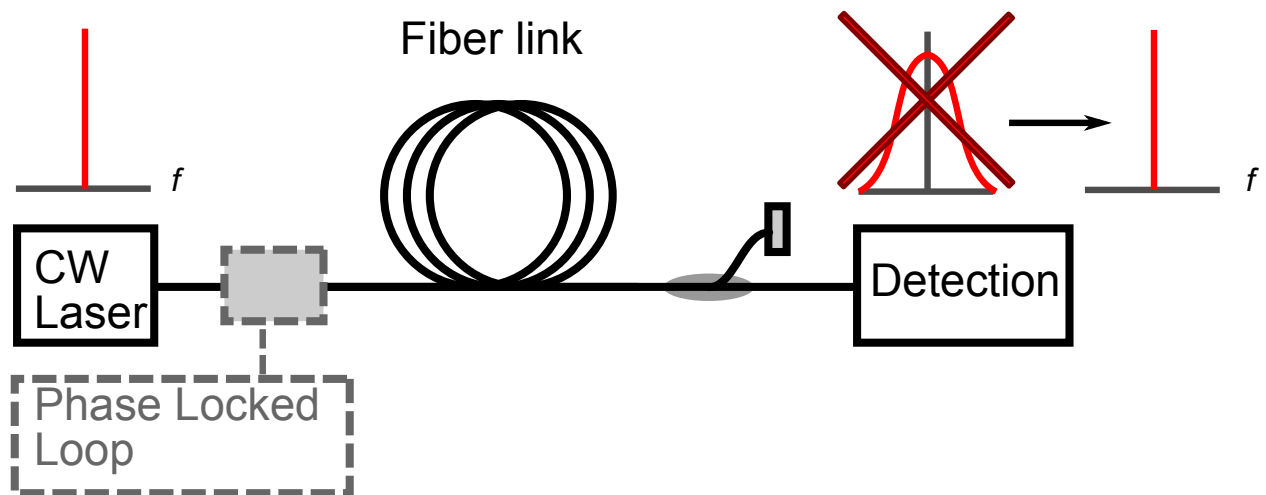

Ultrastable optical frequency transfer over a 5 km fiber link



CHANTAL VAN TOUR

May 30, 2013
Amsterdam

Ultrastable optical frequency transfer over a 5 km fiber link

BACHELOR THESIS

OF

APPLIED PHYSICS AT

THE HAGUE UNIVERSITY OF APPLIED SCIENCES, DELFT

PERFORMED AT THE

LASERLAB VU UNIVERSITY, AMSTERDAM

Author:

C. VAN TOUR

*Supervisors (The Hague University
of Applied sciences):*

DR. A.J. LOCK

DR. L.H. ARNTZEN

Supervisor

(LaserLaB VU University):

DR. J.C.J. KOELEMELJ



May 30, 2013
Amsterdam

Abstract

A laboratory test setup is built to transfer and actively stabilize an ultrastable signal, obtained from a laser with sub-Hz linewidth, through a 5 km long fiber link. The fiber noise is measured and compensated via a feedback loop acting on an AOM that can change the frequency (and therefore the phase) of the light using a beat note between a local oscillator and the round-trip signal as input. The performance of the active noise compensated fiber link is characterized by the beat note between the remote optical frequency and the ultra-stable optical source frequency. The fractional frequency instability of the actively stabilized 5 km link is 1×10^{-18} at 1 s, reaching 4×10^{-20} after 10^3 s of averaging.

Commercial fiber-optic networks for long-distance telecommunication employ optical amplifiers to compensate for attenuation of optical signals. This is typically done using erbium-doped fiber amplifiers (EDFAs) which, however are equipped with optical isolators and cannot be used for bidirectional round trip signals. In this project semiconductor optical amplifiers (SOAs) are studied as an alternative to EDFAs, which can operate outside the gain bandwidth of EDFAs. Inclusion of a bidirectional SOA in the link adds to the frequency instability, but the increase remains less than one order of magnitude over the full range of averaging times. The SOAs are also tested in a quasi-bidirectional configuration where the light coming from different directions are amplified by different SOAs, which introduces 6 m of uncompensated fiber. Nevertheless, the current quasi-bidirectional setup results in a relative frequency instability of 3×10^{-17} at 1 s, reaching 4×10^{-18} after 8×10^3 s of averaging.

For all the configurations tested here, the performance of the active noise compensated fiber link is compared with the instability of a comparison between two high-accuracy optical Al^+ clocks ($2.0 \times 10^{-15} \tau^{-1/2}$) which are currently the most accurate clocks ever built [1]. The 5 km link will not add a significant amount of noise to the comparison of the Al^+ clocks, since the fractional frequency instability of the 5 km link is 2-3 orders of magnitude less than the instability of the Al^+ clocks on a time scale of $1 - 14 \times 10^5$ s for the unamplified and bidirectional amplified links. Even in the sub-optimum case of a quasi-bidirectional amplifier, the link stability remains well below the Al^+ clock stability for averaging times $1-10^4$ s.

The use of SOAs, here demonstrated for the first time, offers the possibility to use wavelengths and amplifiers outside the C-band which is commonly used in commercial optical telecommunication systems. Thus, no valuable C-bandwidth needs be sacrificed for ultrastable frequency transfer, and bidirectional out-of-band 'bypass' amplifiers are made feasible. The results of this project may therefore be useful for future implementations of 'SuperGPS' time and frequency transfer via optical networks.

Contents

Abstract	iii
1 Introduction	1
2 Theory	3
2.1 Frequency-dependent noise	3
2.2 Active compensation of phase noise in fiber links for frequency transfer	6
3 Design of the test link	13
3.1 Michelson-Morley Interferometer	14
3.2 Detection of local and remote signal	15
3.3 Layout of the PLL and VCO	16
4 Methods	17
4.1 Phase noise power spectral density	17
4.2 Allan deviation	18
5 Results and discussion	23
5.1 Performance of the compensated link without optical amplification	23
5.2 Performance of two different configurations for optical amplification	30
6 Conclusion & Outlook	35
7 Bibliography	37
8 Dankwoord	39
A List of components	41
B Acousto-optic modulators	43
B.1 Polarization dependence of the AOM	44
C Gaussian beam waist measurements	47
D Test of the Allan deviation code	49
E Characteristics of the used SOAs	53
F Originele opdrachtomschrijving (Dutch)	55

Chapter 1

Introduction

Recently the project called 'SuperGPS through optical networks' started at the LaserLaB VU. The goal of this project is to transfer time and frequency information of very accurate atomic clocks through existing fiber networks. Where global navigation satellite systems (GNSS) use satellites in the orbit that broadcast radio signals, SuperGPS uses fiber networks for telecommunication to transfer time and frequency information in the form of laser signals. Frequency transfer can be several orders of magnitude more stable in comparison with GNSS [2, 3, 4, 5]. Furthermore, SuperGPS will only need one very accurate atomic clock while each satellite of a GNSS system has its own atomic clock. For example, the Global Positioning System (GPS) uses at least 24 satellites and thereby 24 atomic clocks. Where GNSS does not work well in densely populated places with tall buildings or for example road tunnels, SuperGPS could work by extending the fiber network with antenna masts. These masts can be connected to and synchronized with the fiber network, broadcasting the accurate time and positioning information. SuperGPS could also serve as a back-up system when GNSS does not work.

The time and frequency information of an atomic clock can be converted into a modulated laser that is transported via an optical fiber link. However, temperature fluctuations and acoustic noise in the fiber link will have a negative influence on the stability of the frequency of the light and cause phase noise in the signal. In order to maintain the accurate time and frequency information of the atomic clock throughout the fiber link, the accumulated noise has to be compensated. This project focuses on the frequency stability of the light that travels through such a compensated fiber link.

The noise in the signal is measured by sending part of the light back through the fiber link. The phase of this light will then pick up the disturbance twice, assuming that the fiber round-trip time is much shorter than the characteristic time scale of the phase noise. This disturbance can be measured at the start of the fiber link using a Michelson-Morley interferometer (MMI). The phase noise of the light can subsequently be compensated by means of a feedback loop acting on an acousto-optic modulator (AOM) that can change the frequency (and therefore the phase) of the light.

A test setup is built with a 5 km long optical fiber link between the local and remote end. An ultrastable laser is used as an optical frequency source, since the optical atomic clock is still under construction. Long-haul fiber links are commonly equipped with optical amplifiers to compensate the attenuation of optical signals in long fibers. To simulate these conditions in the lab, the performance of the setup is tested in several configurations with and without semiconductor optical amplifiers (SOA). The phase noise compensation only works when part of the light makes a round-trip through the fiber link. However, commercial fiber networks are built for one-way propagation of the light, because the erbium-doped fiber amplifiers (EDFAs) used have isolators (which protect the amplifier from back-scattered light and prevent unwanted lasing). The operating wavelength range of the EDFAs (1525 nm - 1565 nm) determines the used wavelength range in the fiber network, and is called the C-band. The use of wavelengths outside the C-band for time and frequency transfer has two advantages: firstly, it does not require to sacrifice valuable C-band telecommunication capacity. Secondly, out-of-band wavelengths are readily separated off the C-band wavelengths using optical filters. This allows to bypass EDFAs through custom bidirectional amplifiers for which SOAs may be used, as SOAs can provide gain in a broader wavelength range than EDFAs. So far, however, SOAs have not been used for time and frequency transfer. In this project, SOAs are tested in two different configurations. The

performance of the noise compensated link is characterized with the single sided phase noise power spectral density and the Allan deviation of the transmitted frequency.

Chapter 1 describes the theory of active noise compensation in optical fibers. The design of the test link is described in chapter 2. Mathematical methods used to characterize the performance of the active noise compensation in the test link, are reported in chapter 4. The results in chapter 5 show the performance of the test setup in different configurations, with and without optical amplification.

Chapter 2

Theory

In order to transfer an ultrastable optical frequency signal over a fiber network, it is necessary to compensate for the noise that the phase of the signal picks up in the fiber link. The stability of a transmitted frequency degrades due to temperature fluctuations and acoustic noise in the fiber link. The basic principles of noise are described in section 2.1. Section 2.2 describes how the noise of a transmitted frequency can be compensated.

2.1 Frequency-dependent noise

When monochromatic light of a laser is transferred over a fiber link, the linewidth of the light at the remote end of the link will be broadened. This effect is due to temperature fluctuations and acoustic noise which cause a variation in the optical path length of the fiber link, which may be regarded as an effective random Doppler broadening of the transmitted frequency.

The optical phase, ϕ , of light with a carrier wavelength λ_0 at the end of a fiber link with refractive index n can be written as

$$\phi = nL \frac{2\pi}{\lambda_0} \quad (2.1)$$

with respect to the optical phase of the light at the entrance of the fiber. A change in the temperature, dT , changes the optical phase due to the thermal expansion of the fiber (proportional to $\frac{1}{L} \frac{\partial L}{\partial T}$) and the thermo-optic change in the refractive index (proportional to $\frac{\partial n}{\partial T}$). The optical phase fluctuates due to the temporal temperature fluctuations as

$$\frac{d\phi}{dt} = \frac{2\pi L}{\lambda_0} \left[\frac{\partial n}{\partial T} + \frac{n}{L} \frac{\partial L}{\partial T} \right] \frac{dT}{dt}. \quad (2.2)$$

The thermo-optic and thermal expansion coefficient of the fiber link are in the order of $\frac{\partial n}{\partial T} \approx 10^{-5} \text{ K}^{-1}$ and $\frac{1}{L} \frac{\partial L}{\partial T} \approx 10^{-6} \text{ K}^{-1}$, respectively [6]. The signal that exits the fiber link can be described as a time-varying electric field, $E(t)$, as function of time t with equation 2.3 [7].

$$E(t) = [E_0 + \varepsilon(t)] \cos[2\pi\nu_0 t + \phi(t)] \quad (2.3)$$

where

E_0	electric field amplitude	(V/m)
$\varepsilon(t)$	amplitude deviation	(V/m)
ν_0	nominal frequency of the light	(Hz)
$\phi(t)$	phase deviation	(rad).

The frequency stability of the output signal depends on the phase deviation, $\phi(t)$, of the signal. The total phase of the signal ϕ_{tot} after a time t is

$$\phi_{\text{tot}} = 2\pi\nu_0\tau + \int_0^t \frac{d\phi}{dt}. \quad (2.4)$$

The derivative of ϕ_{tot} gives the instantaneous frequency $\nu(t)$ of the signal,

$$\nu(t) = \nu_0 + \frac{1}{2\pi} \frac{d\phi}{dt}. \quad (2.5)$$

The fractional frequency $y(t)$ is defined as

$$y(t) = \frac{\Delta\nu(t)}{\nu_0} = \frac{\nu(t) - \nu_0}{\nu_0} = \frac{1}{2\pi\nu_0} \frac{d\phi}{dt} = \frac{dx}{dt}, \quad (2.6)$$

where

$$x(t) = \frac{\phi(t)}{2\pi\nu_0}. \quad (2.7)$$

Together with equation 2.2, the fractional frequency can be written as

$$y(t) = \frac{L}{\nu_0\lambda_0} \left[\frac{\partial n}{\partial T} + \frac{n}{L} \frac{\partial L}{\partial T} \right] \frac{dT}{dt}. \quad (2.8)$$

The frequency instability of the signal caused by the fiber link may be due to different kinds of noise that can be distinguished when $y(t)$ or $x(t)$ of the transmitted signal is measured as a function of time. Table 2.1 lists the most common types of noise and their acronyms. The acronym PM stands for phase noise modulation and FM stands for frequency noise modulation. The results in chapter 5 show phase noise power spectral density curves and Allan deviation curves which are able to distinguish between the different types of noise in the signal.

Noise type	Acronym
White PM	(W PM)
Flicker PM	(F PM)
White FM	(W FM)
Flicker FM	(F FM)
Random Walk FM	(RW FM)
Flicker Walk FM	(FW FM)
Random Run FM	(RR FM)

Table 2.1: The different types of phase noise (PM) and frequency noise (FM)

Figure 2.1 shows examples of the behavior of four most common noise types.

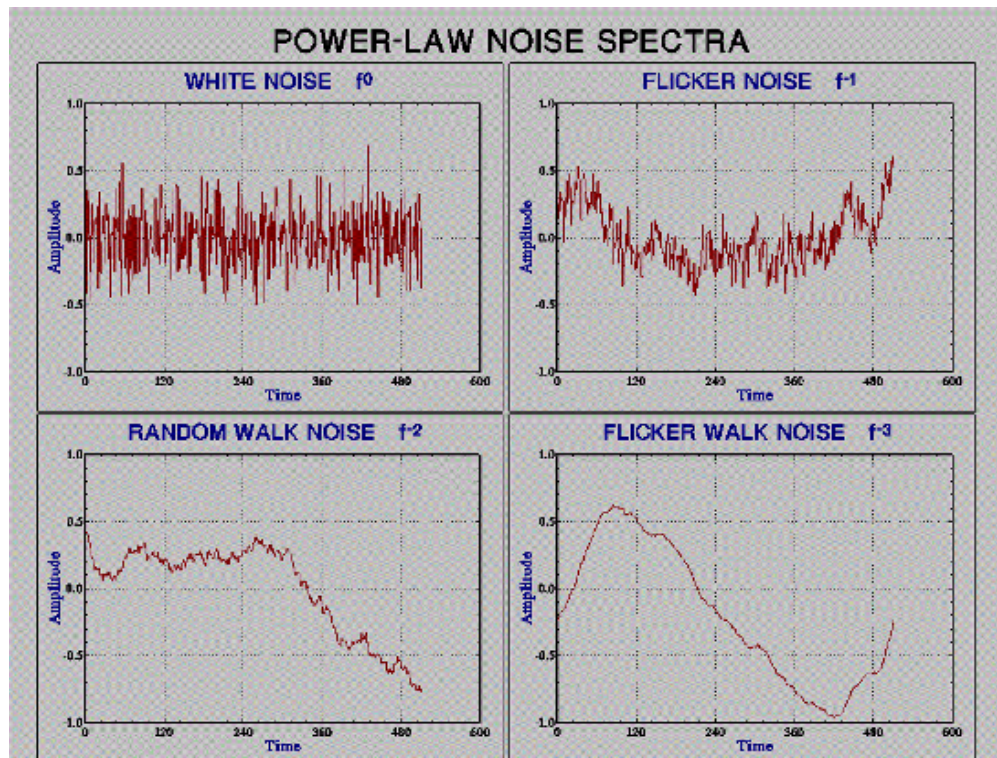


Figure 2.1: Examples of the four most common noise types [7].

2.2 Active compensation of phase noise in fiber links for frequency transfer

It has been shown that it is possible to measure and compensate for the noise acquired by the optical signal during transmission through the fiber [2, 3, 4, 5, 8]. This technique requires that part of the light at the end of the fiber is sent back so as to make a round-trip through the fiber link. The round-trip light provides the error signal to the servo loop that will compensate the noise. This implies that the link should be bidirectional, *i.e.* the light should be able to travel in both directions through the same fiber link. Figure 2.2 shows a simplified scheme of the setup that is built to test the active noise compensation. The whole setup is built on one optical table with a 5 km test link between the local and remote part of the setup. An ultrastable continuous-wave (CW) laser with a linewidth <1 Hz is used as a frequency source. The laser linewidth will be broadened in the fiber link due to temperature fluctuations and acoustic noise as described in section 2.1. The setup in figure 2.2 compensates the phase noise and thereby reduces the laser linewidth broadening.

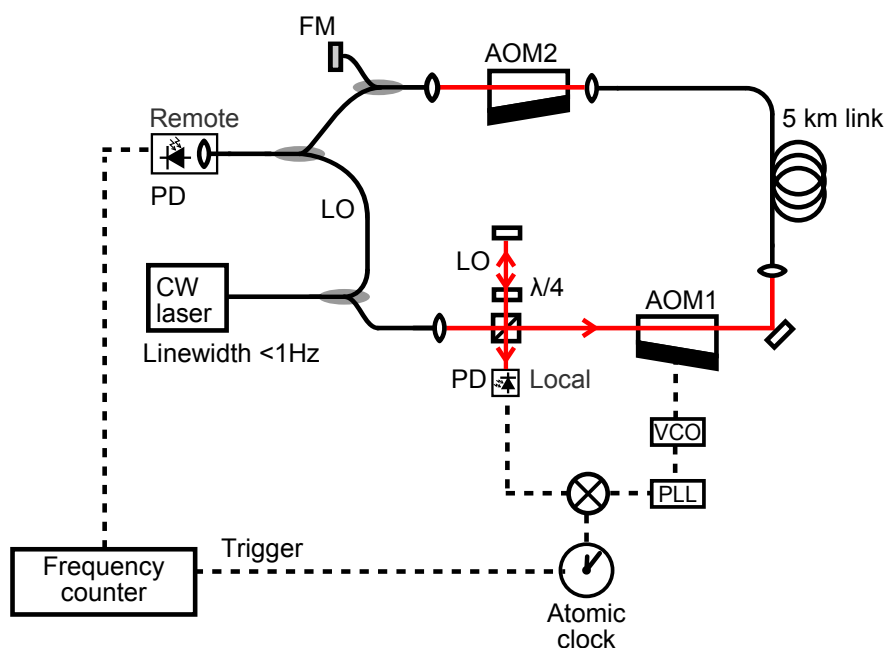


Figure 2.2: Simplified scheme of the setup for active noise compensation in optical fibers. The red lines represent free-space optical beam paths, the black lines are optical fibers and the dashed lines are electrical paths. The round-trip frequency (f_i) is mixed with the local oscillator (LO) on a photodiode. The remote frequency (f_r) is mixed with the LO on a fiber-pigtailed photodiode.

Figure 2.2 shows that part of the laser light is split to serve as a local oscillator (LO) for homodyne detection at the remote end of the fiber (section 2.2.1). The rest of the light is split by a polarizing beam splitter. The reflected light serves as a LO for the homodyne detection at the local end of the fiber. The transmitted light travels subsequently through an acousto-optic modulator (AOM), the 5 km test link, and a second AOM. The first and second AOM cause a frequency shift of the transmitted signal of respectively f_{AOM1} and f_{AOM2} . The principle operation of the AOMs is described in more detail in the appendix, chapter B. Part of the transmitted light is reflected by a Faraday mirror (FM) and travels back through the 5 km link and the two AOMs. This round-trip signal (having a frequency f_i) is mixed with the local oscillator (having a frequency f_{LO}) on a photodiode to produce a periodic electrical signal at the beat frequency of the two optical fields. This signal is commonly referred to as the beat note. The beat note contains twice the frequency difference caused by the AOMs plus twice the phase noise caused by the fiber link. The beat note at the local end forms the input for the phase-locked loop (PLL) and voltage-controlled oscillator (VCO). AOM1 is used to modulate the frequency of the light and is controlled by the PLL and VCO, while AOM2 is used to distinguish the round-trip signal from stray reflections along the fiber link. The remote

signal, f_r , is mixed with the LO on a fiber-pigtailed photodiode to create a beat note at the remote end of the link. This beat note is used to observe the noise reduction achieved by the noise-compensation system.

2.2.1 Beat notes and optical phase detection

Phase detection of optical fields is not straightforward, as no opto-electronic devices exist that are fast enough to detect the field oscillations at $\sim 2 \times 10^{14}$ Hz frequency. However, optical phase detection may be readily achieved by mixing an optical field with the optical field of a LO in a photodiode, which converts the beat note between the fields into an electrical current. This is done here to detect the phases of the local and remote optical fields. This method of phase detection is also referred to as heterodyne detection in the case that the two fields stem from independent sources, and homodyne detection in the case that the two fields originate from the same source while having different phases due to a modulating device in one of the field paths [9]. The superposition of the electric field of the LO, $E_{\text{LO}}(x, t)$ and the round-trip signal, $E_1(x, t)$, can be written as

$$E(x, t) = E_{0,\text{LO}} \cos(k_{\text{LO}}x_{\text{LO}} - \omega_{\text{LO}}t) + E_{0,1} \cos(k_1x_1 - \omega_1t + \phi) \quad (2.9)$$

where k is the wavevector, ω is the angular frequency ($\omega = 2\pi f$), and ϕ is the phase difference between the two waves. Note that the superposition of the electric fields is polarization dependent. Therefore, two beams with orthogonal polarizations will not interfere. The photodiode is sensitive to the irradiance of the beam, $I(x, t)$, which is proportional to $E^2(x, t)$ and may be written as

$$\begin{aligned} I(x, t) \propto E^2(x, t) &= [E_{0,\text{LO}} \cos(k_{\text{LO}}x_{\text{LO}} - \omega_{\text{LO}}t) + E_{0,1} \cos(k_1x_1 - \omega_1t + \phi)]^2 \\ &= E_{0,\text{LO}}^2 \cos^2(k_{\text{LO}}x_{\text{LO}} - \omega_{\text{LO}}t) + E_{0,1}^2 \cos^2(k_1x_1 - \omega_1t + \phi) \\ &\quad + 2E_{0,\text{LO}}E_{0,1} \cos(k_{\text{LO}}x_{\text{LO}} - \omega_{\text{LO}}t) \cos(k_1x_1 - \omega_1t + \phi) \end{aligned} \quad (2.10)$$

Equation 2.10 can be rewritten with goniometric rules which results in

$$\begin{aligned} E^2(x, t) &= \frac{E_{0,\text{LO}}^2}{2} [1 + \cos 2(k_{\text{LO}}x_{\text{LO}} - \omega_{\text{LO}}t)] \\ &\quad + \frac{E_{0,1}^2}{2} [1 + \cos 2(k_1x_1 - \omega_1t + \phi)] \\ &\quad + E_{0,\text{LO}}E_{0,1} \cos[k_{\text{LO}}x_{\text{LO}} + k_1x_1 - (\omega_{\text{LO}} + \omega_1)t + \phi] \\ &\quad + E_{0,\text{LO}}E_{0,1} \cos[k_{\text{LO}}x_{\text{LO}} - k_1x_1 - (\omega_{\text{LO}} - \omega_1)t - \phi] \end{aligned} \quad (2.11)$$

When ω_{LO} and ω_1 are comparable to each other, $\omega_{\text{LO}} \approx \omega_1$, then $(\omega_{\text{LO}} + \omega_1) \gg (\omega_{\text{LO}} - \omega_1)$. The first three terms contain components oscillating at optical frequencies, which are too fast to be detected and contain zero DC power. Therefore, what remains in the photodiode output is the DC offset terms, and the difference frequency component oscillating at $f_{\text{LO}} - f_1$, which is called the beat note. This signal is described in equation 2.11 as

$$E_{0,\text{LO}}E_{0,1} \cos[k_{\text{LO}}x_{\text{LO}} - k_1x_1 - (\omega_{\text{LO}} - \omega_1)t - \phi]$$

where x_{LO} and x_1 both correspond to the position of the photodiode, but are measured with respect to the different beam paths followed by the LO and fiber-link signals. From this expression it is also clear that if the fiber length changes, x_1 will change, leading to an apparent Doppler shift. Likewise, changes in the refractive index will change k_1 and therefore also lead to a time-varying phase shift. The values of k_{LO} , ω_{LO} and ω_1 are assumed to be constant over time, owing to the high stability of the reference laser and interferometer setup used in experiment described in chapter 3.

The frequency of the round-trip signal, f_1 , is shifted twice by AOM1 and AOM2, and picks up the phase noise in the link twice. f_1 can be described as

$$f_1 = f_{\text{LO}} + 2f_{\text{AOM1}} + 2f_{\text{AOM2}} + 2\delta f_{\text{link}} \quad (2.12)$$

where the picked-up phase noise during one round-trip is described as $2\delta f_{\text{link}}$. Here, $\delta_{\text{link}} = \delta_{\text{link}}(t) = (k_{\text{LO}}x_{\text{LO}} - k_1(t)x_1(t))$, as explained above. The frequency of the laser is assumed to be stable within the time delay between the round-trip signal and the LO. Furthermore, the picked up phase noise is assumed to be stationary within one round-trip time, which justifies multiplying δ_{link} with a factor two to obtain the round-trip phase noise from the one-way phase noise. The local photodiode detects a beat note Δf_1 of

$$\Delta f_1 = f_1 - f_{\text{LO}} = 2(f_{\text{AOM1}} + f_{\text{AOM2}} + \delta f_{\text{link}}). \quad (2.13)$$

Similarly, the remote photodiode detects a beat note Δf_r of

$$\Delta f_r = f_r - f_{\text{LO}} = f_{\text{AOM1}} + f_{\text{AOM2}} + \delta f_{\text{link}} \quad (2.14)$$

The phase-locked loop (PLL) and voltage-controlled oscillator (VCO) use the beat note of the local signal to measure and compensate for the phase noise during one round-trip. Note that the round-trip causes a delay in the feedback that will limit the noise suppression. The remote signal is detected to test the stability of the remote frequency when the noise-compensation system is operational.

2.2.2 Phase-locked loop and voltage-controlled oscillator

The phase of the beat note signal on the local end of the setup, Δf_1 , is compared with the phase of the output of an atomic clock by using a frequency mixer, see figure 2.3. The atomic clock is used as an accurate reference frequency for the servo loop that compensates the fiber noise. The frequencies of the two AOMs are chosen so that

$$f_{\text{clock}} = 2(f_{\text{AOM1}} + f_{\text{AOM2}}). \quad (2.15)$$

Here, f_{clock} is the output frequency of the clock. Equation 2.13 is used to determine the frequency output of the mixer, f_m ,

$$f_m \equiv \Delta f_1 - f_{\text{clock}} = 2(f_{\text{AOM1}} + f_{\text{AOM2}} + \delta f_{\text{link}}) - 2(f_{\text{AOM1}} + f_{\text{AOM2}}) = 2\delta f_{\text{link}}. \quad (2.16)$$

This equation shows that the mixer output contains the phase noise caused by the fiber link during one round-trip. As explained in detail below, the output of the mixer is used by the PLL to change the frequency of AOM1 via the VCO, so that $f_m \rightarrow 0$ and $f_{\text{AOM1}} \rightarrow (f_{\text{AOM1}} - \delta f_{\text{link}})$.

Figure 2.3 depicts a schematic servo loop. The mixer converts the detected phase noise to a voltage. This

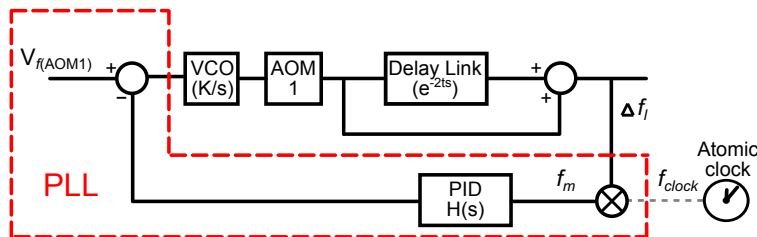


Figure 2.3: Schematic of the servo loop. The components within the red dashed box are referred to as the PLL. Shown also are the components (in Laplace notation) of the servo loop; a proportional-integral-derivative controller (PID), voltage-controlled oscillator (VCO), delay of the signal due to the link. The link delay takes into account the action of AOM1 on the light entering the fiber link, including the round-trip delay that occurs before detection at the local photodiode. The loop bypassing the link delay represents the action of AOM1 on the return light from the fiber link, which arrives with virtually zero delay at the photodiode. The combined effect of these two actions of AOM1 on the local photodiode is modeled by the voltage adder after the link.

voltage is forwarded to the input of the PID controller. The output voltage of the PID controller is added to a DC voltage, $V_{f(\text{AOM1})}$, and the summed voltages are fed into the input of the VCO. The VCO converts its input voltage to an RF voltage that controls AOM1. The PID controller adjusts its output voltage so that the input voltage of the PID controller becomes minimal, thereby compensating the link noise. The open loop gain of the system, $G(s)$, (in LaPlace notation) is

$$G(s) = K \frac{1}{s} (1 + e^{-2\tau s}) G_0 C(s) \quad (2.17)$$

where

K	Gain of the VCO	(V/Hz)
$\frac{1}{s}$	Pure integrator term due to the VCO	(-)
$e^{-2\tau s}$	Delay of the link where τ is the delay for one-way propagation	(-)
G_0	Gain of the mixer	(Hz/V)
$C(s)$	PID transfer function	(-).

Here, $s = j\omega$ where j is the complex number $\sqrt{-1}$ and ω is the frequency of the input signal. The VCO works as a pure integrator which can be seen as follows. Suppose the input of the VCO is a constant voltage V , corresponding to a stationary phase difference $\Delta\phi$. Then, the output phase of the VCO is $\phi_{\text{out}} \propto \int_0^t V dt' \propto \int_0^t \Delta\phi dt'$. A Bode plot can be used to characterize the frequency response of $G(s)$ in terms of magnitude by calculating the absolute values of equation 2.17 and in terms of phase by calculating the argument of equation 2.17. An example of a phase Bode plot with the characteristics of $G(s)$ is shown in figure 2.4, where the PID controller is off, *i.e.* $C(s) = 1$. The pure integrator of the VCO causes the phase plot to start at $-\pi/2$ rad for $\omega = 0$, since

$$\arg \left[\frac{1}{s} \right] = \arg \left[\frac{1}{j\omega} \right] = \arctan(-\infty)$$

and

$$\lim_{x \rightarrow -\infty} \arctan(x) = -\pi/2 \text{ rad.}$$

The system tends to show oscillatory behavior for frequencies above the critical frequency for which the phase in the Bode plot passes $-\pi$ rad. At the critical frequency, the noise spectrum of the system then exhibits a feature commonly called the servo spike. The curve of the Bode plot can be written as $\arg[G(s)] = -(\pi/2 + 2\pi f\tau)$, passing through $-\pi$ rad at the frequency of the servo spike, $f_s = 1/(4\tau)$ [5]. From this equation, it is clear that the control bandwidth of the system depends on the delay caused by the link. The system becomes unstable when $G(s)$ is > 1 at the frequency of the servo spike where $\arg[G(s)] = -\pi$.

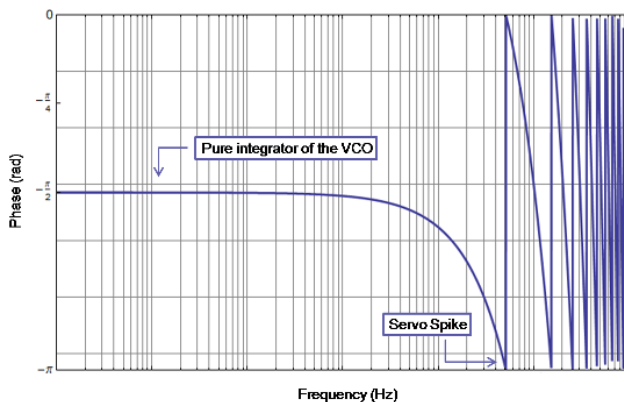


Figure 2.4: Example of the phase as a function of frequency in the open loop gain.

In principle, it is possible to stabilize the system by only using the gain, K_p , of the PID controller. However, the integrator and differentiator of the PID controller can make the response of the phase-locked loop faster. The integral term is proportional to the magnitude of the error signal as well as the duration of the error. The error is integrated over a certain time, τ_i , and added to the output of the PID controller. The derivative term is proportional to the slope of the error signal over a certain time, τ_d . This signal is added to the output of the PID controllers. $C(j\omega)$ can be described in terms of the P, I and D transfer functions, see table 2.2 [10]. $C(j\omega)$ is then given by

	$H(j\omega)$	$\text{abs}[H(j\omega)]$	$\text{arg}[H(j\omega)]$
P	K_p	K_p	0
I	$\frac{1}{j\omega\tau_i}$	$\frac{1}{\omega\tau_i}$	$-\frac{\pi}{2}$
D	$j\omega\tau_d$	$\omega\tau_d$	$\frac{\pi}{2}$

Table 2.2: The transfer functions, $H(j\omega)$, of the PID-controller

$$C(j\omega) = G_{\text{PID}} \left(K_p + \frac{1}{j\omega\tau_i} + j\omega\tau_d \right) \quad (2.18)$$

where G_{PID} the overall gain of the PID-controller is. Figure 2.5 represents an example of the magnitude Bode plot and phase Bode plot of a PID-controller with $G_{\text{PID}} = 1$, $K_p = 3$ dB, $\tau_i = 0.5$ s and $\tau_d = 0.1$ s. The integral term causes a phase shift of $-\pi/2$ in the phase Bode plot, but the magnitude Bode plot drops

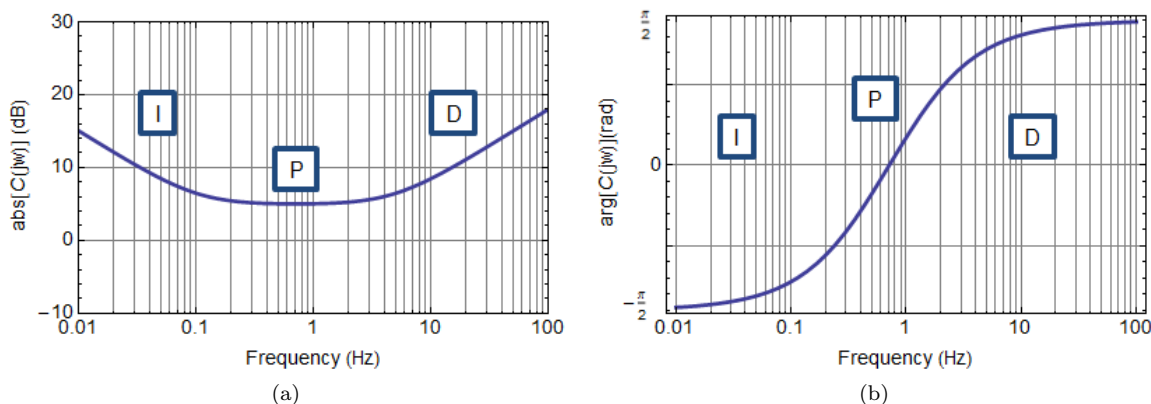


Figure 2.5: Typical (a) Magnitude Bode plot and (b) phase Bode plot of a PID-controller.

with 6 dB/octave due to the integration term which makes it possible to set the gain of the PID-controller

higher without making the system unstable. Note that the system becomes unstable when $G(s)$ is > 1 at the frequency of which $\arg[G(s)] = -\pi$. The magnitude Bode plot increases with 6 dB/octave because of the differential term, but the phase bode plot goes to $+\pi/2$ which again makes it possible to set the gain of the PID-controller higher, thereby increasing the control bandwidth of the feedback system. The lay-out of the VCO and PLL that are used in this project are discussed in section 3.3.

optical input power of the local photodiode is 10 mW. The used fibers are angle cleaved (FC-APC). The AOMs are described in detail in the appendix, chapter B. The polarization controller in the local part of the setup is used to control the ratio between the amount of reflected and transmitted light on the polarization beam splitter. The polarization controller in the remote part of the setup is used to control the polarization state of the light that travels through AOM2. The test link consists of two free-space AOM setups that are almost identical, except for the short arm of the Michelson-Morley interferometer (LO).

3.1 Michelson-Morley Interferometer

The Michelson-Morley Interferometer (MMI) compares the phase of the round-trip signal to the LO. Figure 3.2 shows the test setup of the MMI.

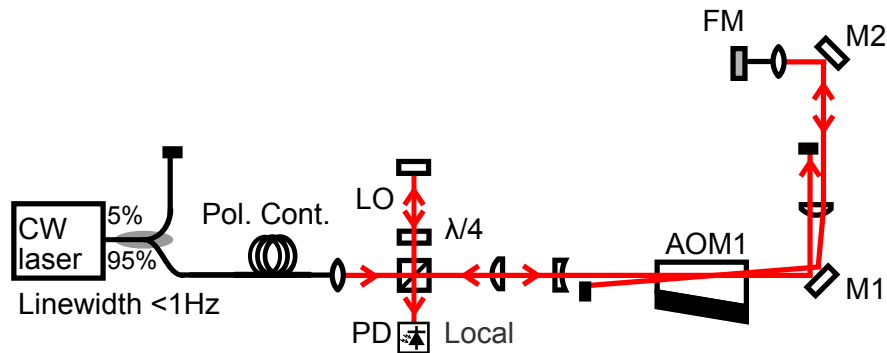


Figure 3.2: The design of the Michelson-Morley interferometer where the LO and the round-trip signal create a beat note. This test setup consists of one AOM and no test link. The red lines represent optical free-space beam paths and the black lines are optical fibers.

95% of the laser light travels through the MMI. This beam is split by a polarizing beam splitter into two beams with orthogonal polarizations. The polarization controller is used to change the ratio of the amount of reflected and transmitted light on the beam splitter. The light in the short arm of the MMI reflects off the beam splitter, travels through a quarter wave plate and is reflected back by a plane mirror. The beam is subsequently transmitted by the polarizing beam splitter, because the polarization is rotated by $\pi/2$ by the two passes through the quarter wave plate and the intermediate reflection. The light in the long arm of the MMI travels through a telescope, AOM1 and a focusing lens. The light reflects off a Faraday mirror (FM) and travels back to the beam splitter. The Faraday mirror rotates the polarization of the light by $\pi/2$. Due to this rotation the beam will be reflected towards the photodiode by the polarizing beam splitter. Before reaching the photodiode, the light makes a second pass through AOM1, thus acquiring twice the AOM frequency shift. The signals of the short and long arm of the MMI interfere on the local photodiode and create a beat note.

A telescope and a cat's eye reflector are used in both free-space setups [11]. The telescope and cat's eye are depicted in detail in figure 3.3.

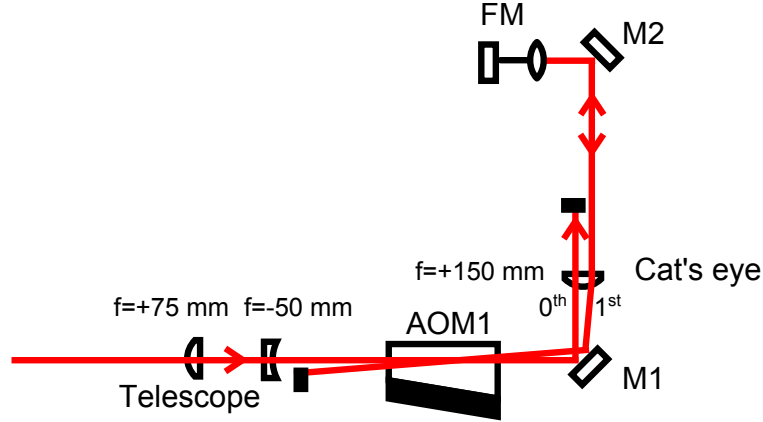


Figure 3.3: The telescope and cat's eye lens configuration for the setup with AOM1. The setup with AOM2 has the same configuration. Note that the combination of M2, the fiber incoupling lens, the fiber and the FM act as a retroreflector here.

A telescope is used to create a light field with a planar wavefront inside the AOM. The plano-convex lens of the telescope has a focal distance of $f_1 = 75$ mm and the plano-concave lens has a focal distance of $f_2 = -50$ mm. The combination of these two lenses make it possible to focus the beam inside the AOM, so that the waist, w_0 , of the beam is inside the AOM. This is crucial for the efficiency of the AOM, because the radius of curvature of the light field is most planar only at w_0 . The position and size of w_0 (defined as the beam radius for which the intensity has dropped off by $1/e^2$) are measured using the knife-edge method. A detailed description of these measurements can be found in the appendix, chapter C.

Note that in figure 3.3, the combination of M2, the fiber incoupling lens, the fiber and the FM act as a retroreflector within the cat's eye arrangement. The configuration of the cat's eye reflector has two advantages as opposed to using a plane mirror. When the distance between the AOM and the plano-convex lens ($f_c = 150$ mm) is equal to the focal distance of the lens, the 0th and 1st order of the AOM become parallel behind the lens as can be seen in figure 3.3. Both beams will strike the retroreflector at normal incidence; consequently, both beams are reflected back in the same way as they came. The cat's eye lens maintains the reciprocal beam paths even if the AOM frequency (and thereby the diffraction angle) is tuned over a large range. The retroreflector is placed at a distance from the lens equal to the focal distance of the lens. In this configuration w_0 is imaged on the second mirror, so that the beam path back to the AOM is fully reciprocal, and the waist is again located at the AOM. This is the second advantage of this configuration.

3.2 Detection of local and remote signal

The local signal is detected free space with an APD3320A avalanche photodiode. The frequency of the local beat note is given by equation 2.13,

$$\Delta f_l = 2(f_{\text{AOM1}} + f_{\text{AOM2}} + \delta f_{\text{link}}) = 2(156.25 \times 10^6 - 151.25 \times 10^6 + \delta f_{\text{link}}) = (10 \times 10^6 + 2\delta f_{\text{link}}) \text{ Hz}$$

The remote signal is detected with a fiber-pigtailed photodiode. The frequency of the remote beat note is given by equation 2.14,

$$\Delta f_r = (f_{\text{AOM1}} + f_{\text{AOM2}} + \delta f_{\text{link}}) = 156.25 \times 10^6 - 151.25 \times 10^6 + \delta f_{\text{link}} = (5 \times 10^6 + \delta f_{\text{link}}) \text{ Hz}$$

3.3 Layout of the PLL and VCO

The local beat note signal (Δf_l) is mixed with a 10 MHz signal of a rubidium clock as depicted in figure 3.4. The output frequency of the mixer, f_m , fluctuates around 0 Hz and so does the output voltage of the mixer (0 V).

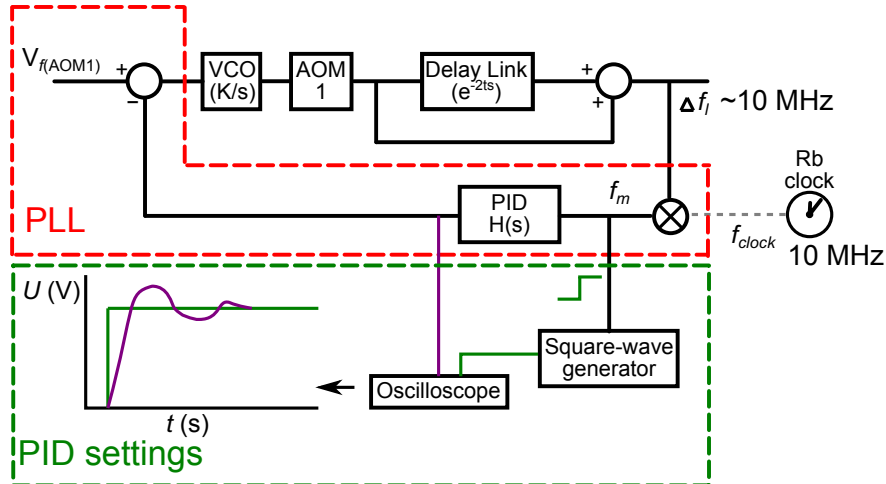


Figure 3.4: Schematic of the servo loop. The components within the red dashed box are referred to as the PLL. Shown are the components of the servo loop; a proportional-integral-derivative controller (PID), voltage-controlled oscillator (VCO), delay of the signal due to the link and a rubidium (Rb) clock. The components within the green dashed box are used to set the PID controller.

The optimum settings of the PID-controller can be found using methods as those presented in textbooks such as Tietze & Schenk or Ziegler & Nichols [10, 12]. These methods derive values for the proportional, integral and derivative term from the oscillation gain and frequency of the system, which are readily measured. The oscillation gain is found by increasing the gain (without I and D action) until the system begins to oscillate. This effect can be seen using an oscilloscope or spectrum analyzer. The gain and the frequency corresponding to the oscillation can be measured, whereafter the P, I and D can be set according to one of these methods. However, these methods are designed for a second order servo loop. Furthermore, these methods are only approximations. Both methods were tested with this setup, but neither of them produced the optimum result.

The PID controller is set using a square-wave voltage that is added to the input of the PID controller, figure 3.4 (b). The square-wave voltage is connected to an oscilloscope together with the output signal monitor of the PID controller. The oscilloscope is triggered by the square-wave voltage. The response of the system can now be viewed on the oscilloscope. First, the P gain is set until the system begins to oscillate whereafter the gain is reduced until the system is stable. Then, the I and D time constants are set using the same steps. The overshoot of the signal should not be more than $\sim 4\%$ and the settling time should be as fast as possible. Typical settings of the PID controller are presented in table 3.1.

Link	G_{PID} (dB)	K_p (%)	τ_i (ms)	τ_d (μs)
1 m	13-14	100	0.6	0.127
5 km	13-14	100	1.3	0.127

Table 3.1: Typical PID settings of the 1 m and 5 km link. The 1 m link is used in the experiments that are described in chapter 5 to determine the noise floor of the active compensated fiber.

The nominal output frequency of the VCO is 156.25 MHz with an operating bandwidth of 20 kHz, which is large enough to phase lock the local beat note signal to the rubidium clock.

Chapter 4

Methods

Two methods are used to determine the performance of the active noise compensated fiber link, as described in the previous sections. The first method consists in measuring the phase noise power spectral density of the remote signal. This method is typically used to characterize the stability of the link on short time scales (< 1 s). The Allan deviation is used to characterize the stability of the remote signal on long time scales ($1 - 10^5$ s). This chapter describes the basics of these two methods.

4.1 Phase noise power spectral density

The phase noise power spectral density (PSD) of the remote signal characterizes the frequency instability in the Fourier frequency domain. A phase noise PSD shows the intensity of the phase or frequency fluctuations as a function of the Fourier Frequency. In order to obtain the phase noise PSD, the frequency of the remote beat note signal, ν , is measured within time intervals of $\Delta t = 1 \mu\text{s}$. The measurements are performed with a frequency counter that has no dead-time and a so-called Π windowing function, *i.e.* no additional averaging takes place by the counter within the $1 \mu\text{s}$ gate time, which might lead to an unwanted artificial reduction of the PSD. The total duration of the measurement T is

$$T = N\Delta t, \quad (4.1)$$

where N is the number of measurements. The maximum Fourier frequency is determined by the Nyquist sampling theorem which states that the maximum frequency equals half the sampling rate, $1/\Delta t$. The power spectral density $S_y(f)$ is calculated for the fractional frequency values, y_n , with

$$S_y(f) = \frac{(\Delta t)^2}{T} \left| \sum_{n=1}^N y_n e^{-i2\pi f n} \right|^2. \quad (4.2)$$

The fractional frequency values are calculated with equation 2.6. It is common to express the power spectral density in terms of phase, $S_\phi(f)$. $S_y(f)$ and $S_\phi(f)$ via the relation,

$$S_\phi(f) = \left(\frac{\nu_0}{f} \right)^2 S_y(f). \quad (4.3)$$

It is even more common to express the power spectral density of the phase in dB,

$$S_{\phi,\text{dB}}(f) = 10 \log^{10}[S_\phi(f)]. \quad (4.4)$$

Using equation 4.4, the slope α of the PSD ($S_y(f) \sim f^\alpha$) provides information about the noise types present in the signal.

4.2 Allan deviation

The Allan deviation is a statistical tool to calculate the fractional frequency instability σ_y of the link versus averaging time τ . The Allan deviation is used here to characterize the fractional frequency instability of the remote signal on a time scale of up to 10^5 s. In analogy with the phase noise power spectral density, the slope of the Allan deviation versus τ contains information about the noise types present in the signal. Many variations of the Allan deviation exist; however, only the three most commonly used Allan deviations are employed here, namely the normal, overlapping, and modified Allan deviations. The modified Allan deviation is used for the end results of this project. The advantage of the modified Allan deviation is that it is capable of distinguishing between white phase noise and flicker phase noise, in contrast to the other two Allan deviations [7].

The frequency, ν , of the remote beat note signal is measured with a Π -type frequency counter as a function of time, with gate time τ_0 . The fractional frequency values are calculated with the help of equation 2.6. The normal Allan deviation (ADEV), $\sigma_y(\tau)$, in terms of frequency data is then defined as

$$\text{ADEV } \sigma_y(\tau) = \sqrt{\frac{1}{2(M-1)} \sum_{i=1}^{M-1} [\bar{y}_{i+1} - \bar{y}_i]^2} \quad (4.5)$$

where \bar{y}_i is the i th of M fractional frequency values averaged over the sampling interval, τ . The sampling interval is given by

$$\tau = m\tau_0 \text{ with } m = 1, 2, \dots, N/2 \text{ and } M = \frac{N}{m} \quad (4.6)$$

Here, N is the number of measurements. An obvious disadvantage is that the useful data set is restricted to powers of two, so that in some cases a substantial part of the frequency data cannot be included in the ADEV calculation.

Strictly speaking, the confidence intervals (error bars) of the normal, overlapping and modified Allan deviations are determined by chi-squared distributions, which are characterized by an equivalent number of degrees of freedom. The number of degrees of freedom depends on the noise type, the averaging factor and the number of data points. In this project, use is made of a commonly-used approximation of the standard deviation of the normal Allan deviation, $\pm\sigma_y(\tau)/\sqrt{M}$ with a confidence interval of 68 % [7]. Note that this approximation is more accurate for short averaging times, where the number of frequency data points is large, and the corresponding chi-squared distribution approximates a normal distribution. For the longest averaging times τ , however, the 'true' chi-squared confidence interval will become more asymmetric (with extended error bars in the upward direction), and the simple approximation used here will be less accurate.

The overlapping Allan deviation (ODEV) makes maximum use of the dataset by calculating all possible overlapping samples, where the samples of the normal Allan deviation do not overlap. The difference between the normal and overlapping Allan deviation is depicted in figure 4.1, where an example is shown with a dataset using an averaging factor of $m = 3$. The modified Allan deviation (MDEV) does not only overlap the samples, but it also performs an extra averaging step so that the difference between white phase noise and flicker phase noise can be observed.

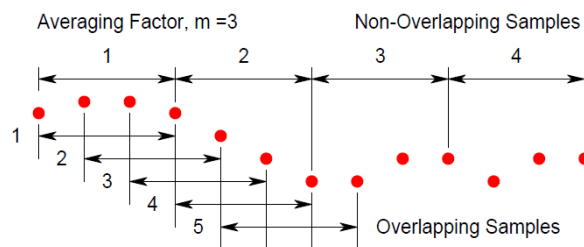


Figure 4.1: An example of the normal Allan deviation versus the overlapping Allan deviation. In contrast to the normal Allan deviation, the overlapping Allan deviation makes use of the whole dataset [7].

The MDEV as a function of τ is defined as

$$\text{MDEV } \sigma_y(\tau) = \sqrt{\frac{1}{2m^4(N-3m+2)} \sum_{j=1}^{N-3m+2} \left[\sum_{i=j}^{j+m-1} \left[\sum_{k=i}^{i+m-1} [y_{k+m} - y_k] \right] \right]^2} \quad (4.7)$$

where y_i is the i th of N fractional frequency values and τ is the sampling interval. Since the calculation of the MDEV involves three summations of which two are computationally intensive inner summations, the fractional frequency data is first integrated to phase data. This allows equation 4.7 to be written as

$$\text{MDEV } \sigma_y(\tau) = \sqrt{\frac{1}{2m^2\tau^2(J-3m+1)} \sum_{j=1}^{J-3m+1} \left[\sum_{i=j}^{j+m-1} [x_{i+2m} - 2x_{i+m} + x_i] \right]^2} \quad (4.8)$$

using phase data instead of fractional frequency data (here, $J = N + 1$). The summations of the Allan deviations are performed 2^n times with $n = 0 \dots \log_2 N$. Calculations of the MDEV for time series of $\tau = 2^{14} = 16384$ s take ~ 10 minutes on a 2012 laptop using Mathematica 8.0.4. For longer time series it might be useful to use ODEV since this calculation is much faster. The ODEV requires ~ 5 seconds to calculate a dataset of 16384 s. The ODEV as a function of τ , ODEV $\sigma_y(\tau)$, is defined as

$$\text{ODEV } \sigma_y(\tau) = \sqrt{\frac{1}{2(J-2m)\tau^2} \sum_{i=1}^{J-2m} [x_{i+2m} - 2x_{i+m} + x_i]^2}. \quad (4.9)$$

Calculations of the modified and overlapping Allan deviation are performed in Mathematica and are tested with 2 test suites provided by the National Institutes of Standards and Technology (NIST) [7]. The test results can be found in the appendix, chapter D.

4.2.1 Phase noise power spectral density and Allan deviation in fiber links

Similar to the PSD described in section 4.1, Allan deviations $\sigma_y(t)$ may be converted to a log-log scale (or, equivalently, be plotted in a log-log plot). In this case, the slope of the normal, overlapping and modified Allan deviation can be described with $\sim \tau^{\mu/2}$ where $\mu = -\alpha - 1$. Table 4.1 gives an overview of the different types of noise together with the slopes of the phase noise PSD and Allan deviation calculations. This table will be used to identify the different types of noise observed in the measured signals presented in sections 5.1 and 5.2.

	S_y		MDEV $\sigma_y(\tau)$	ADEV & ODEV $\sigma_y(\tau)$
Noise type	α	μ	$\mu/2$	$\mu/2$
White PM (W PM)	2	~ -2	$-3/2$	-1
Flicker PM (F PM)	1	-2	-1	-1
White FM (W FM)	0	-1	$-1/2$	$-1/2$
Flicker FM (F FM)	-1	0	0	0
Random walk FM (RW FM)	-2	1	$1/2$	$1/2$
Frequency drift	-3	2	1	1

Table 4.1: The different types of phase noise modulation (PM) and frequency noise modulation (FM) together with the slopes of the PSD and ADEV curves [7].

Table 4.1 shows that the MDEV has different slopes for white phase noise and for flicker phase noise, respectively, while these two types of noise have the same slope for the ADEV and ODEV. Figure 4.2 shows the results of using the three different Allan deviations on the same dataset. From this figure together with table 4.1, it is clear that results obtained with the normal and overlapping Allan deviation can not be compared with results that are obtained with the modified Allan deviation without any correction or notification [13]. Figure 4.3 represents the theoretical phase noise power spectral density diagram and the

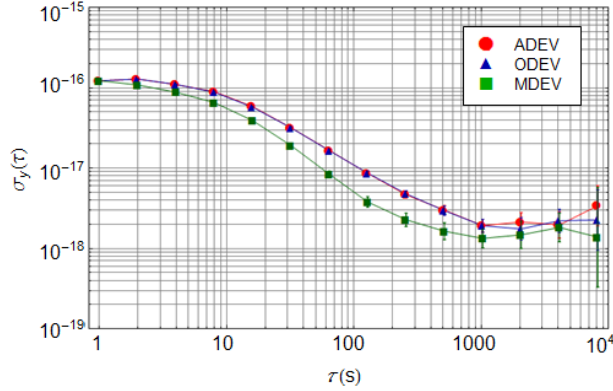


Figure 4.2: Comparison of the normal (ADEV), overlapping (ODEV) and modified (MDEV) Allan deviation using a single dataset of 30 000 s obtained with a gate time of 1 s.

modified Allan deviation diagram for a noise-compensated fiber link [5]. The experimental data will be compared with the theoretical curves of the plots.

Figure 4.3 (a) shows the curve of the expected modified Allan deviation when the active noise-compensation system is operational, *i.e.* when the local beat note signal is phase locked to the rubidium clock. Figure 4.3 (b) shows the phase noise power spectral density for the free-running (unlocked) local signal and the phase locked local signal. The plots are dominated by delay-unsuppressed noise and interferometric noise. The delay-unsuppressed noise is a fundamental limit since after the servo loop acts on the optical signal entering the fiber link through AOM1, it takes time for the light to travel through the fiber link and reach the servo loop 'sensor' (the local photodiode). The interferometric noise is caused by optical path length variations in the local oscillator arm of the MMI due to temperature fluctuations and acoustic noise. The noise in the local oscillator arm of the local and remote MMI cannot be compensated but may be reduced by minimizing the environmental disturbances. As derived previously by Williams *et al.*, the delay-unsuppressed noise $S_D(f)$

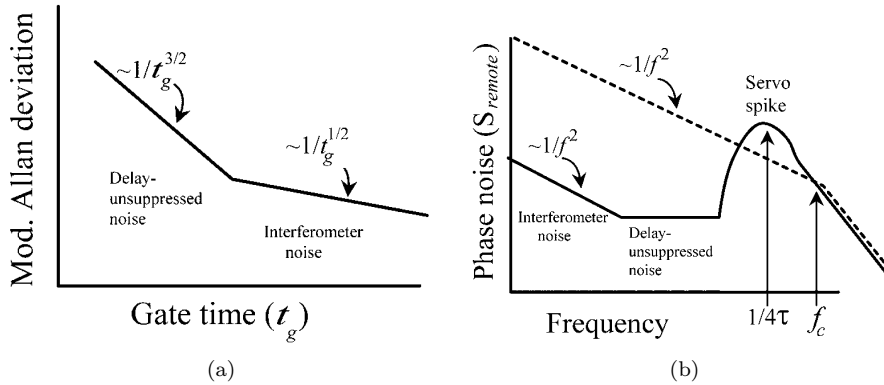


Figure 4.3: The theoretical limit of (a) the Allan deviation and (b) the phase noise PSD plots when the signal is phase locked, according to Williams *et. al.* [5]. The dashed curve in (b) shows the result for the unlocked signal.

on the locked remote signal can be approximated using

$$S_D(f) \approx \frac{1}{3}(2\pi f\tau)^2 S_{\text{fiber}}(f) \quad (4.10)$$

where $S_{\text{fiber}}(f)$ is the phase noise in the transmitted signal and τ is the delay caused by the fiber link [5]. $S_{\text{fiber}}(f)$ scales with $\sim h/f^2$ for $f < f_c$, where h is the phase noise coefficient, and f_c is an empirical cut-off frequency above which $S_{\text{fiber}}(f)$ has been observed to drop off faster than $1/f^2$. This coefficient can also be written as a function of the length of the fiber link, $h_L = h/L$, since h scales with the length L of the link.

The Allan deviation as well as the phase noise PSD are used to determine the noise type and noise level in the signal as a function of averaging time or Fourier frequency. By using these two methods, the obtained results can also be compared with the results of other studies.

Chapter 5

Results and discussion

The results of the active noise compensated fiber link are discussed in this chapter. The link performance is assessed by computing Allan deviations and phase noise power spectral densities of the remote and local beat note signals, which were described in the previous chapters. The results of the compensated link without optical amplification are shown in section 5.1. In section 5.2 the results of a comparison between two different schemes for optical amplification in the fiber link using semiconductor optical amplifiers are presented.

5.1 Performance of the compensated link without optical amplification

The performance of the active noise compensated 5 km fiber link is compared with the results of the unlocked link, and with results obtained from other studies [2, 5].

The first prototype design of the phase noise compensated fiber link is depicted in figure 5.1. The local interferometer is built with free-space components while the remote interferometer is fiber-coupled. Most of the 5 km fiber link is inside a box of which the lid is always open. The rest of the setup is not protected from temperature fluctuations and acoustic noise in the laboratory. Such disturbances also include air currents in the laboratory, produced by cooling fans of running equipments, that may disturb the interferometers. The local and remote detection experience a temperature fluctuation of (1.2 ± 0.2) K (1-day measurement, obtained using a simple thermocouple thermometer).

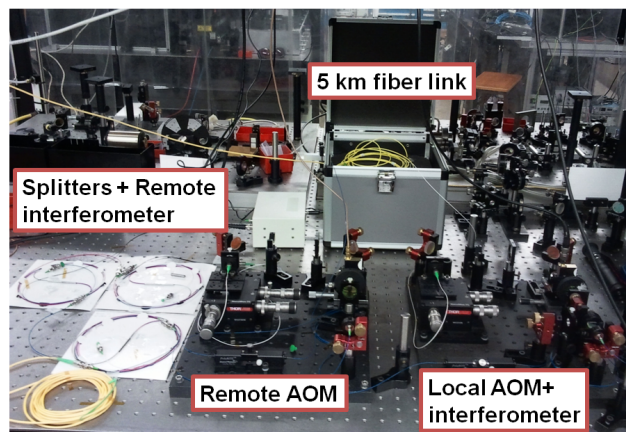


Figure 5.1: The first prototype design of the setup. The interferometers are not protected from the environment.

The first measurement of the setup was performed at the local end of the fiber link (since the remote end was not built yet) when the local beat note signal is not phase locked, *i.e.* the noise compensation system was switched off. Figure 5.2 (a) shows the frequency deviation of the remote signal during one weekend (216 000 s). Figure 5.2 (b) depicts the overlapping Allan deviation (the dataset was too large for the MDEV computer algorithm to process in a reasonable amount of time). The ODEV shows white frequency noise ($\tau = -1/2$) at the first 100 seconds. The peak at 1000 seconds might be due to the controller time constant

of the laboratory heating system, but this would require further investigation. Figure 5.3 shows the phase

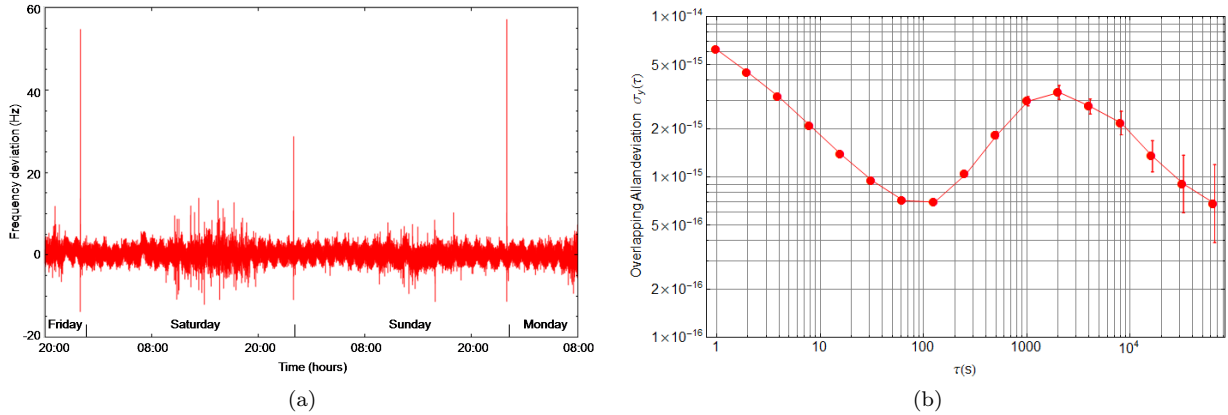


Figure 5.2: The data of the unlocked link measured at the local end of the setup with a II-type frequency counter. (a) The frequency deviation as a function of time. The measurement was taken over the weekend. Outliers are identified as those events that are statistically unlikely (given the distribution of the majority of the data points), and subsequently removed. (b) The overlapping Allan deviation calculated with the data shown in figure 5.2. The data points are interconnected to guide the eye.

noise PSD spectra of the remote signal for the free-running and phase locked local signal of the 5 km link. The data of the unlocked link is fitted with $S_{\text{fiber}}(f) \sim h/f^2$, for Fourier frequencies between 10 – 1000 Hz. This approximation gives a comparison with the result from Williams *et. al* [5]. The phase noise coefficient of the fit is $h = (8 \pm 5) \times 10^1 \text{ Rad}^2\text{Hz}$ (3σ). The phase noise coefficient per unit length of the link is then $h_L = (2 \pm 2) \times 10^1 \text{ Rad}^2\text{Hz/km}$ (3σ). Williams *et. al.* found a value of $\sim 4 \text{ Rad}^2\text{Hz/km}$ which is within the boundaries of the obtained result. A possible explanation for the smaller value found by Williams *et. al.* is that their link incorporates relatively long lengths ($\sim 200 \text{ km}$) of spooled fiber, which may be more immune to acoustic noise than exposed fiber patches. Furthermore, the phase noise spectrum of the unlocked link shows an increase of the negative slope at Fourier frequencies $> 1000 \text{ Hz}$ which agrees with the empirical cut-off frequency f_c also found by Williams *et. al.* (see also figure 4.3).

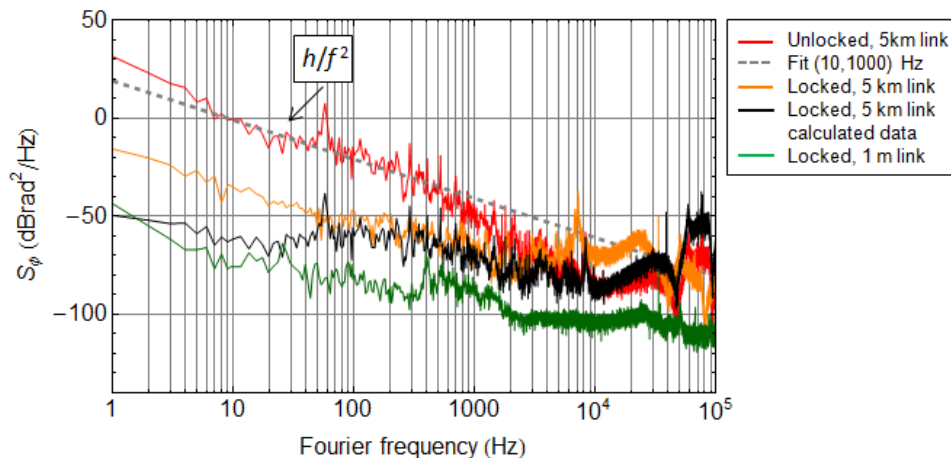


Figure 5.3: Phase noise PSD spectra of the uncompensated and noise compensated 5 km prototype fiber link. The gray dashed line is a fit of the red line (unlocked link). The black curve is the calculated expected 5 km locked fiber link PSD, whereas the actual (measured) PSD is represented by the orange curve. The green curve shows the noise floor of the system obtained by using a 1 m link instead of the 5 km fiber link.

The black curve in figure 5.3 shows the delay unsuppressed noise, $S_D(f)$, which is calculated using equation 4.10 and based on the unlocked PSD of the 5 km link, $S_{\text{fiber}}(f)$ [5]:

$$S_D(f) \approx \frac{1}{3}(2\pi f\tau)^2 S_{\text{fiber}}(f).$$

The delay (τ) due to the fiber link (24, 49 μs) is given by $\tau = \frac{nL}{c}$, where n (1.4682) is the refractive index of the fiber, L (5000 m) is the length of the fiber, and c (299 792 458 m/s) is the speed of light. The extra length of the link due to the splitters and polarization controllers are neglected in this calculation. Figure 5.3 shows that the phase noise of the calculated data is lower than the phase noise of the measured data. This indicates that the phase-locked loop might not have been optimal. However, this calculation is a rough approximation. Moreover, this calculation is only legitimate for the delay-unsuppressed noise. This fact can also explain why the difference between the calculated and real data is minimal between Fourier frequencies of roughly 50-3000 Hz. The servo-spike is observed at ~ 7 kHz. The theoretical frequency of the servo spike is ~ 10 kHz, calculated with equation $f = 1/(4\tau)$. This means that the control bandwidth of the noise compensation system is less than the theoretical limit. The difference in the calculated frequency and the observed frequency of the servo spike may be due to additional phase rotation by the electronics used to control the AOM. However, most of the link noise occurs at frequencies below 1 kHz, implying that the control bandwidth is well sufficient.

Figure 5.4 shows the Modified Allan deviation for datasets of 30 000 seconds, measured at the remote end of the fiber link. The MDEV gives a relative frequency instability of 1×10^{-16} at 1 s, reaching 5×10^{-19} after 8×10^3 s for the 1 m link. For the 5 km link, the MDEV calculations give a relative frequency instability of 1×10^{-16} at 1 s, reaching 1×10^{-18} after 8×10^3 s. The first 10 seconds of the MDEV show flicker frequency noise (τ^0), whereafter the MDEV curve drops with τ^{-1} which indicates flicker phase noise. The slope of the MDEV shows flicker frequency noise at > 1000 seconds.

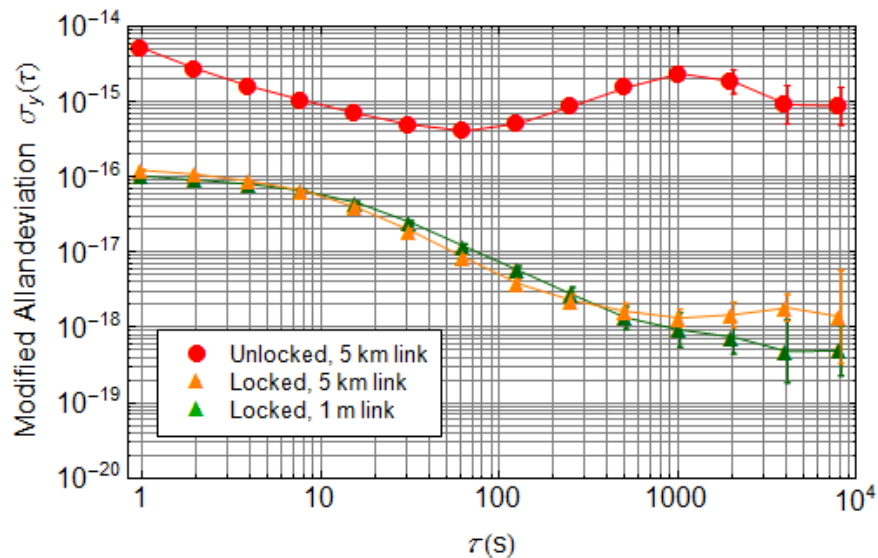


Figure 5.4: The modified Allan deviation for the uncompensated 5 km link (red circles), the noise compensated 5 km link (orange triangles), and 1 m link (green triangles) as a noise floor reference. The uncompensated 5 km link was measured at the local end of the setup.

The measurements with the 1 m link can be interpreted as the noise floor of the setup. The MDEV calculations show that the theoretical limit of the fractional frequency instability is not reached, because the fiber link experiences flicker frequency noise. It is shown in [2] that the maximal fractional frequency instability of the noise floor can reach 3.5×10^{-21} after 4000 seconds with a slope of τ^{-1} (normal Allan deviation). This fractional frequency instability is not reached with this setup, mainly because the uncompensated (out

of loop) optical paths are not protected from temperature fluctuations and acoustic noise. Figure 5.5 depicts the optical paths that are not compensated by the phase-locked loop. The 2 m of fiber to the Faraday mirror is part of the loop, but not part of the link so these fibers will also add uncompensated phase noise to the signal. Shortening the uncompensated optical paths would enhance the performance of the setup. Since the used fibers can not be shortened during this project, the temperature fluctuations and the acoustic noise near the uncompensated optical paths is minimized in order to obtain better results.

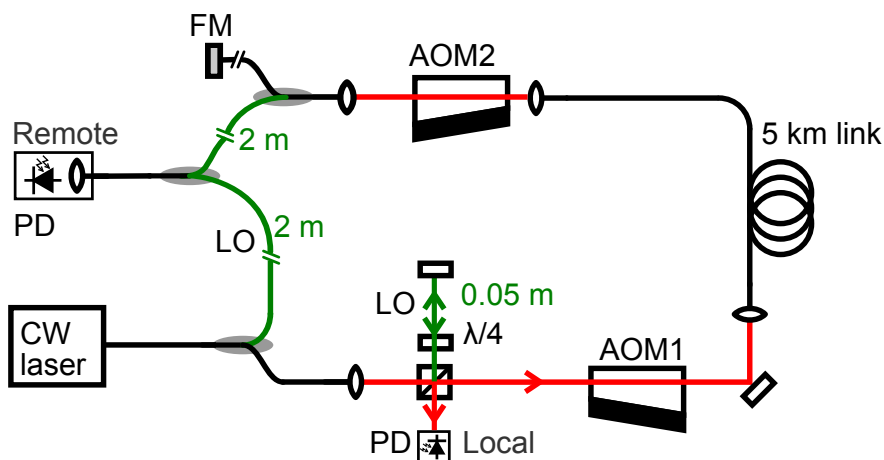


Figure 5.5: The simplified scheme of the setup (without the electronics) where the green paths are uncompensated by the PLL.

In a second version of the link setup, a wooden box lined with acoustically damping material is placed over the whole setup, apart from the link as depicted in figure 5.6. The temperature fluctuations inside as well as outside the box are measured as shown in figure 5.7. The resolution of the temperature sensor is 0.1 K and the accuracy is 0.5 K. These measurements show that the temperature of the laboratory is more stable during the night than during the day. The temperature fluctuation in the box is within the resolution of the temperature sensor of 0.1 K. It is also clear that the temperature inside the box is more stable than outside the box.

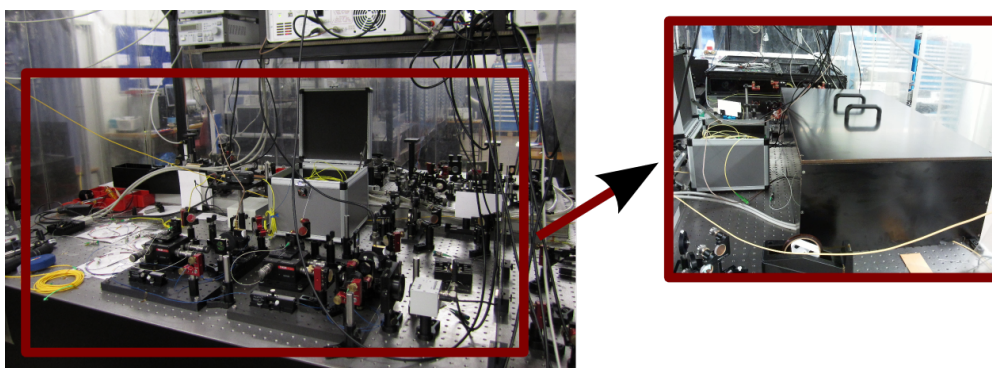


Figure 5.6: Two configurations of the setup: on the left the prototype setup where the interferometers are not covered is shown whereas on the right the second setup is shown, where the whole setup, apart from the 5 km link, is placed inside a wooden box with damping material inside.

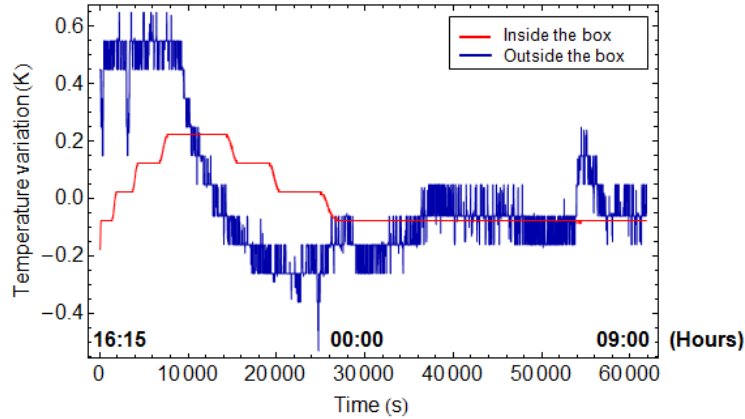


Figure 5.7: The temperature inside and outside the box is measured with two different (same type) temperature sensors at the same time. The resolution of the temperature sensors is 0.1 K and the accuracy is 0.5 K.

Temperature fluctuations in out-of-loop paths lead to fractional frequency fluctuations according to equation 2.2 and 2.6 in section 2.1. For example, a temperature fluctuation of 1 K over 24 hours affecting the 4 m of uncompensated fiber on the remote end causes a fractional frequency fluctuation of $\sim 10^{-18}$ whereas a fluctuation of 0.01 K over 10 s causes a fractional frequency fluctuation of $\sim 10^{-16}$ which would well explain the MDEV observed in figure 5.4 at time scales 1-10 s.

The performance of the active noise compensate link is characterized with the phase noise PSD and the modified Allan deviation. Figure 5.8 shows the phase noise spectra of measurements with and without the box.

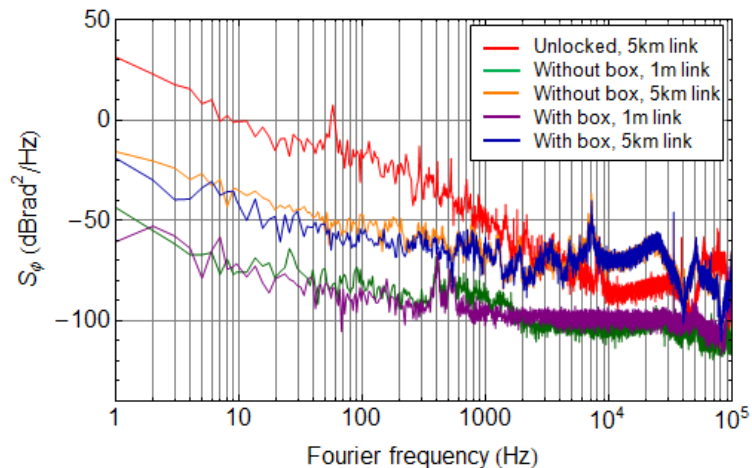


Figure 5.8: Phase noise PSD spectra of the uncompensated 5 km prototype link, and of the noise compensated 5 km and 1 m link, with and without the wooden box with acoustic damping material.

The phase noise PSD spectra of the measurements with the box reveal some noise suppression at Fourier frequencies < 2000 Hz as compared to the setup without the box. At higher Fourier frequencies, the phase noise spectra with the box become similar to those without the box. The modified Allan deviation curves for datasets of 3×10^4 s are presented in figure 5.9. The relative frequency instability of the 1 m link is now 4×10^{-19} at 1 s, reaching 2×10^{-20} after 10^3 s with the box. The MDEV shows frequency drift ($\sim \tau^1$) at higher averaging times which causes the frequency instability to rise to 2×10^{-19} after 8×10^3 s of averaging. The MDEV for the 5 km link is 1×10^{-18} at 1 s, reaching 4×10^{-20} after 10^3 s and 2×10^{-19} after 8×10^3 s. The frequency drift, on a time scale of $10^3 - 10^4$ s, may be caused by the residual temperature fluctuations inside the box. The out-of-loop paths should be shortened to obtain results with fractional frequency instabilities $< 10^{-20}$.

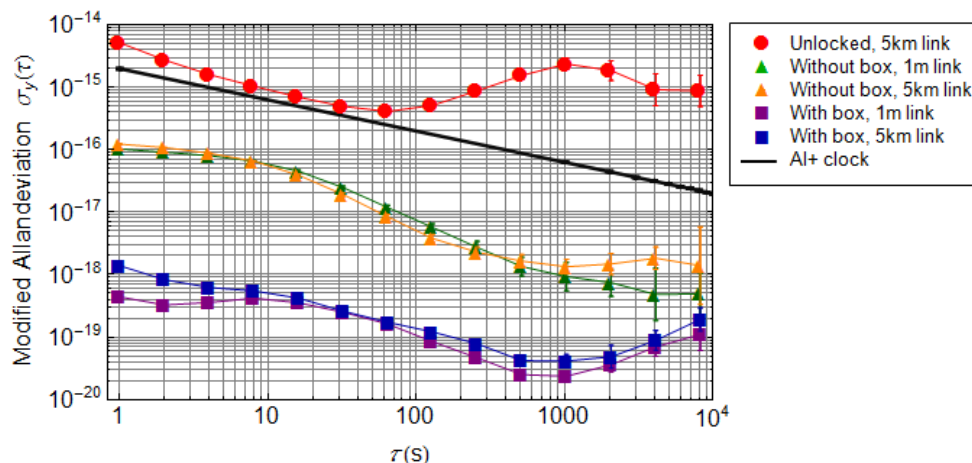


Figure 5.9: The relative frequency instability of the remote signal calculated with the MDEV for the uncompensated 5 km link, and the noise compensated prototype 5 km and 1 m link. The black line represents the fractional frequency instability for a comparison between two Al^+ clocks [1].

The overlapping Allan deviation is used to calculate the relative frequency instability at averaging times $> 10^4$ s. Figure 5.10 depicts the overlapping Allan deviation curves for datasets with a length between $8 \times 10^4 - 14 \times 10^4$ s. These curves show that the frequency drift is not observed for averaging times $> 2 \times 10^4$ s.

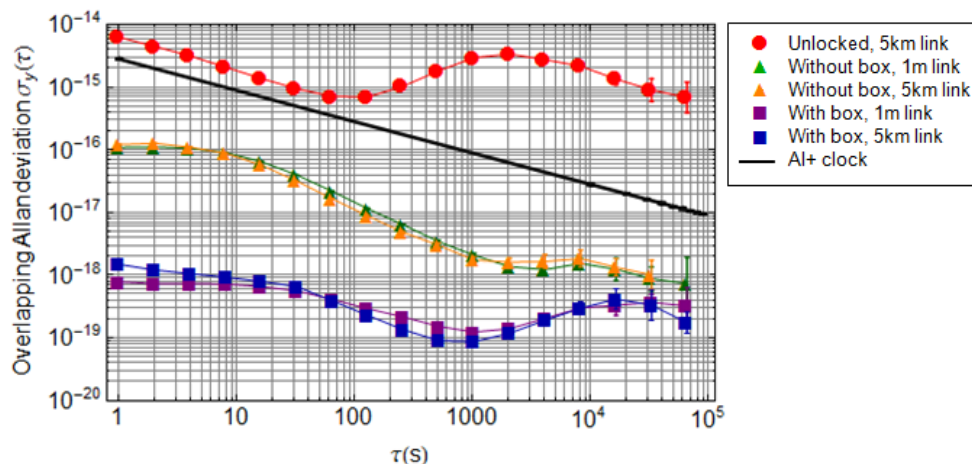


Figure 5.10: The relative frequency instability of the remote signal calculated with the ODEV for the uncompensated 5 km link, and the noise compensated prototype 5 km and 1 m link. The black line represents the fractional frequency instability for a comparison between two Al^+ clocks [1].

Compensated fiber links will be used for comparisons of two ultrastable laser sources at different and widely separated locations (for example, two ultrastable lasers each of which is locked to an Al^+ optical clock). The frequency stability of such a comparison is due to the sum of the relative frequency fluctuations of the Al^+ clocks themselves, and those of the (compensated) fiber link. For such clock comparisons, it is therefore important that the link contribution remains well below the relative instability of the two clocks. The black line in figure 5.9 represents the fractional frequency instability for a comparison between two high-accuracy optical Al^+ clocks [1]. The fractional frequency uncertainty of one Al^+ clock is 8.6×10^{-18} . The ODEV of the comparison gives an instability of $2.8 \times 10^{-15} \tau^{-1/2}$, which is reached only after relatively long averaging times. The ODEV and the MDEV calculations are related by $\text{MDEV} = \text{ODEV} \times 2^{-1/2}$ for a slope of $\tau^{-1/2}$ [13]. The instability of the MDEV is thus given by $2.0 \times 10^{-15} \tau^{-1/2}$. The fractional frequency instability of the unlocked link is larger than the fractional relative frequency instability of two Al^+ clocks. This means that the unlocked link is not well suited for transferring the accurate time and frequency of the Al^+ clock. However, the fractional frequency instability of the phase locked 5 km link (with and without the box) is 2-3 orders of magnitude smaller than the instability of the Al^+ clock. The 5 km link would therefore not add a significant amount of phase noise to the comparison between the two high-accuracy optical Al^+ clocks.

5.2 Performance of two different configurations for optical amplification

The optical signal of the laser is attenuated due to losses in the fiber link. The attenuation in typically-used fibers is ~ 0.2 dB/km. The test link of 5 km causes a power loss of ~ 1 dB which does not need to be amplified in this setup. However, optical amplifiers will be needed when the fiber link is longer and the power of the local or remote signal becomes too low to detect with a sufficient signal-to-noise ratio. As is mentioned in the introduction, erbium-doped fiber amplifiers (EDFA) are used in optical fiber networks but are not used in this project. EDFAs have an operating wavelength range of 1525 -1565 nm [14], which is determined by the EDFA gain spectrum. The wavelength range that is used in fiber networks is based on the operating wavelength of the EDFAs and is called the C-band. However, commercial fiber networks are built for one-way propagation of the light, because the EDFAs have isolators which prevent the amplifier from lasing when operating at high (25-30 dB) gain. Because of these isolators, the light can not travel back and forth through the same fiber as required for the noise compensation presented here. To circumvent this, schemes have been developed to route a particular C-band wavelength for time and frequency transfer through a bidirectional bypass amplifier (see [3] and references therein). Alternatively, the amplifiers may be bypassed using a certain wavelength range outside the C-band, which has the additional advantage that no valuable telecommunication bandwidth needs be sacrificed. Amplification of out-of-band wavelengths may be achieved using semiconductor optical amplifiers (SOA) which have a broader wavelength operating range than EDFAs. These optical amplifiers are tested in two different configurations which are shown in figure 5.11.

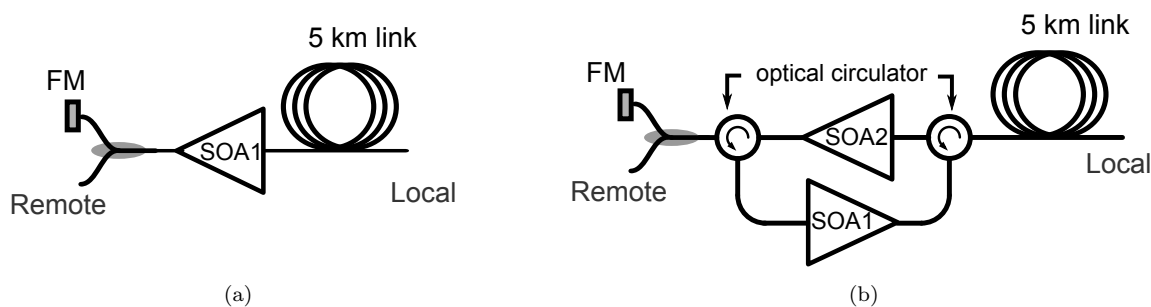


Figure 5.11: (a) Bidirectional scheme of the test link with one SOA and (b) a quasi-bidirectional scheme of the test link with two SOAs.

Figure 5.11 (a) displays the bidirectional schema where the light is amplified in both directions by the same SOA. The advantage of this scheme is that the light picks up the same phase noise in both directions (apart from noise faster than the time in between the two passes). The disadvantage of this scheme is that any back reflection from fiber connections as well as Rayleigh back-scattered light in the link may be amplified as well, which might lead to unwanted lasing of the amplifier. Typically this is solved by reducing the gain to values below 25 dB. Here it should be noted that the two propagation directions could have a different optical frequencies when AOM2 is placed between SOA1 and the FM (which is not the case for this project). The quasi-bidirectional configuration depicted in figure 5.11 (b) uses two SOAs and two optical circulators which prevent the amplification in other directions. In principle this scheme suffers from the same drawback as the scheme in figure 5.11; however, narrowband spectral filters might be used before and after each SOA to prevent unwanted back-scattered light from entering either SOA, so that the amplifiers might be operated at high gain. The disadvantage of this scheme is that the optical path is not fully reciprocal, so that differential optical path length variations in the amplifier are not entirely compensated. It is this limitation that is investigated here. It is therefore important to shield any uncompensated lengths of fiber as much as possible from temperature fluctuations and acoustic noise, so that the disturbance is minimal.

The performance of the SOAs is characterized as a function of the bias current, I , that is applied to the SOAs. The power of the amplified light is measured with a fiber-pigtailed power meter. This power meter also contains a variable attenuator for the light that passes through the meter. The power of the

amplified light is measured with and without blocking the light of the laser. When the laser light is blocked, the measured power is that of the amplified spontaneous emission (ASE) of the SOA; with the laser light present, the measured power contains both the amplified optical signal and the ASE. For simplicity, the ASE power level is assumed to be independent of the optical signal power. However, this may not be necessarily the case. The results can be found in the appendix, chapter E. The actual power of the signal can then be calculated with equation 5.1.

$$P_{s, \text{SOA}}(I) = P_{\text{SOA}}(I) - P_{\text{ASE}}(I) \quad (5.1)$$

where P_{SOA} is the total power with the laser optical signal present and P_{ASE} is the power measured when the laser is blocked. Since the power meter measures the power in dBm, equation 5.1 can be written as

$$P_{s, \text{SOA}}(I) \text{ (dBm)} = 10 \log_{10} [10^{P_{\text{SOA}}(I) \text{ (dBm)}/10} - 10^{P_{\text{ASE}}(I) \text{ (dBm)}/10}] \quad (5.2)$$

which is used for the results. Figure 5.12 depicts $P_{s, \text{SOA}}$ as a function of I for the two SOAs. In order to

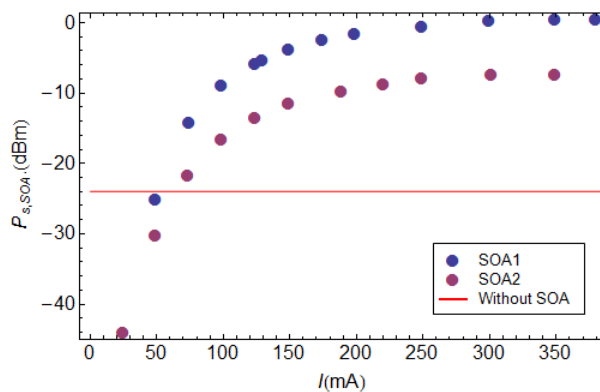


Figure 5.12: The output power of the signal, $P_{s, \text{SOA}}$, as a function of the bias current, I , through the SOAs. The red line depicts the signal power, P_s , when no SOA is used.

calculate the gain of the SOA, the input power of the light should have also been measured. Since one power meter was available, the gain is calculated in an alternative fashion. The SOA is taken out of the setup and the power of the light (P_s) is measured again. The red line figure 5.12 represents this measurement. The gain of the SOA as a function of I is then

$$\text{Gain} = \frac{P_{s, \text{SOA}}(I) \text{ (mW)}}{P_s(I) \text{ (mW)}}$$

$$\text{Gain (dB)} = P_{s, \text{SOA}}(I) \text{ (dBm)} - P_s(I) \text{ (dBm)}$$

As a first test, SOA1 is used in the bidirectional scheme with $I = (380.10 \pm 0.01)$ mA. The gain of the optical signal is then ~ 24 dB. The data sheet of SOA1 gives a maximum gain of 20 dB, less than the 24 dB that is measured. However, the gain is dependent on the input power of the beam which could have been different for the measurements on the data sheet. The attenuation of the power meter is set so that the power of the local signal is the same as without optical amplification, so that the link stability results can be compared to the results of the case without optical amplification. The local signal is phase locked and the remote signal of the fiber link is measured over 4 days. Figure 5.13 (a) shows that the amplitude of the frequency deviations as a function of time varies over the weekend. The exact reason for this is unknown, possible sources are the instability of the ultrastable laser and variations in the bias current of the SOA.

Figure 5.13 (b) shows the results of the MDEV for two different datasets of 3×10^4 s and the ODEV of the entire dataset, obtained using the 5 km link including one bidirectional SOA. Since there are significant differences between the two datasets of 3×10^4 s, significant differences between the frequency stabilities of the two datasets are visible. The best dataset is used for comparison with other results in figures 5.15 and 5.17 (b), anticipating that it will be possible to find (and remove) the source of the variations seen in the time series of the frequency data (figure 5.13(a)).

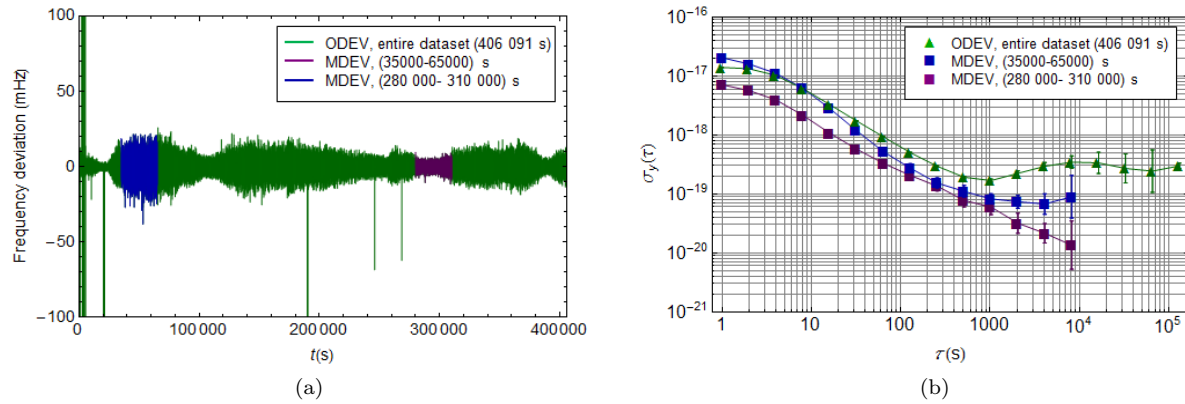


Figure 5.13: The performance of the noise compensated 5 km link including a single bidirectional with a semiconductor optical amplifier (SOA). The dataset (a) covers 4 days. The MDEV in (b) is calculated for 2 different datasets; the worst and the best case scenario. The ODEV is used to calculate the fractional frequency instability of the whole dataset.

The phase noise PSD for the 5 km link and the 1 m link with and without the SOA are depicted in figure 5.14. There is no noticeable difference between the phase noise spectra obtained with and without the SOA. This indicates that any phase noise added by the SOA must be either relatively slow (> 1 s) or fast ($< 10 \mu\text{s}$).

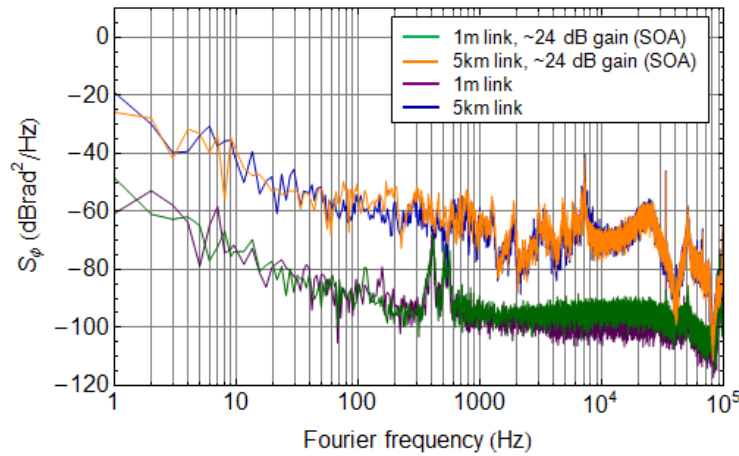


Figure 5.14: Phase noise PSD spectra of the noise compensated prototype 5 km and 1 m fiber link with and without a single bidirectional SOA. All measurements are performed with the wooden box.

The modified Allan deviation curves for datasets of 3×10^4 s with and without the SOA are depicted in figure 5.15.

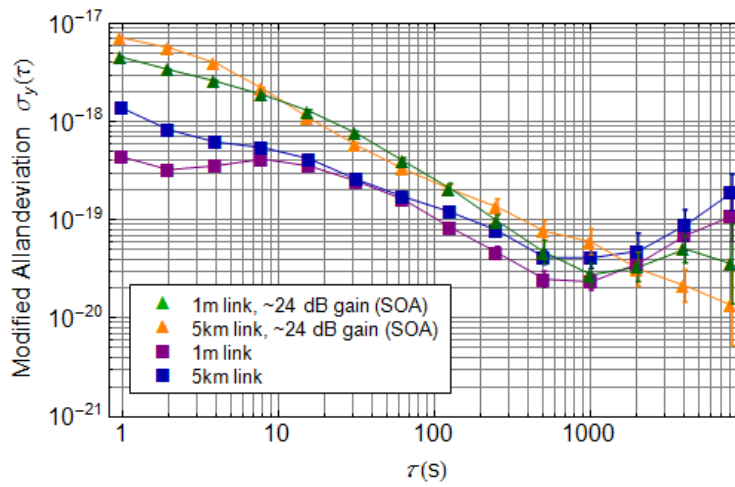


Figure 5.15: The relative frequency instability of the noise compensated prototype 5 km and 1 m link are both measured with and without a single bidirectional SOA. All measurements are performed with the wooden box.

At an averaging time of 1 s, the relative frequency instability of the 1 m link with the SOA is 5×10^{-18} as opposed to 4×10^{-19} without a SOA. The relative frequency instability of the 5 km link at 1 s with the SOA is 7×10^{-18} as opposed to 1×10^{-18} without a SOA. The SOAs obviously add noise at averaging times $< 2 \times 10^3$ s. Nevertheless, the relative frequency instability of the 1 m link with the SOA reaches 3×10^{-20} after 8×10^3 s. The relative frequency instability of the 5 km link with the SOA reaches 1×10^{-20} after 8×10^3 s. These results show that SOAs can be used to amplify ultrastable optical frequency signals for comparisons of the most accurate optical clocks.

The SOAs are also tested in the quasi-bidirectional scheme depicted in figure 5.11 (b). Each circulator has three fiber pigtailed of 1 m length. The total length of uncompensated fiber due to this setup is 6 m. The uncompensated fibers cannot be placed inside the wooden box, because this would require that also the SOAs themselves are placed in the box, which would lead to unwanted temperature variations induced by the Peltier elements used to stabilize the temperature of the SOAs. Instead, the uncompensated fibers are placed in two separate boxes of cardboard. The gain of SOA2 limits the maximal round-trip gain of the signal, see figure 5.12. The settings used in the frequency measurements in this arrangement are listed in table 5.1.

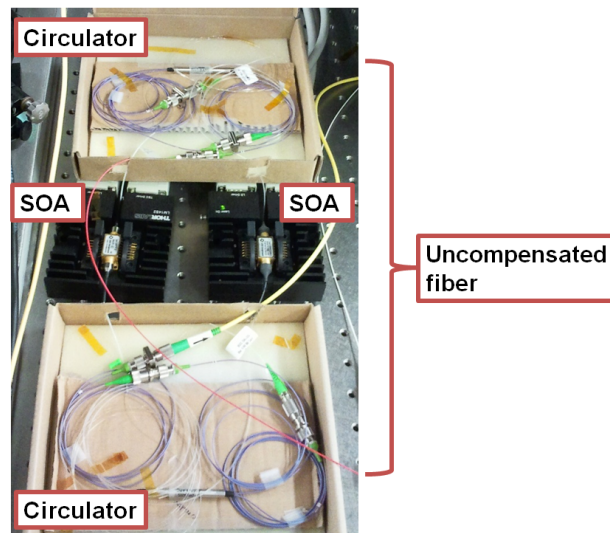


Figure 5.16: The quasi-bidirectional setup with two SOAs and two circulators with fibers of 1 m length. The boxes of cardboard are closed during the measurements.

The two SOAs are supposed to amplify the light with the same amount of gain. However, the power as a function of the current through the SOAs (figure 5.12) was measured only after the phase noise PSD and MDEV measurements were performed. The results shown in table 5.1 indicate a difference of (4.5 ± 0.4) dB in the settings of SOA1 and SOA2. In future follow-up experiments, this difference should of course be removed. Just as with the bidirectional scheme, the attenuation of the power meter is set so that the power of the local signal is the same as without optical amplification in order to make a fair comparison with the unamplified link data. The phase noise PSD of this quasi-bidirectional scheme is compared with

	Direction	I (mA)	Gain (dB)
SOA1	Backward	130.28 ± 0.01	18.7 ± 0.2
SOA2	Forward	189.5 ± 0.05	14.2 ± 0.2

Table 5.1: The settings of the SOAs that are used in the quasi-bidirectional configuration.

the PSD obtained with the bidirectional scheme (figure 5.17 (a)). The phase noise PSD for the 1 m link in the quasi-bidirectional scheme is larger than in the bidirectional scheme over the whole Fourier frequency range. However, the PSDs obtained for the 5 km links show no significant difference. The MDEV curves in figure 5.17 (b) show that both the 1 m and the 5 km links give rise to a higher fractional frequency instability when using the quasi-bidirectional scheme than using the bidirectional scheme. This difference is likely caused by the extra 6 m of uncompensated fiber link which is only partly shielded from environmental changes in the laboratory. Still, the fractional frequency instability of the bidirectional setup as well as the quasi-bidirectional setup are lower than the fractional frequency instability of the comparison between two optical Al^+ clocks.

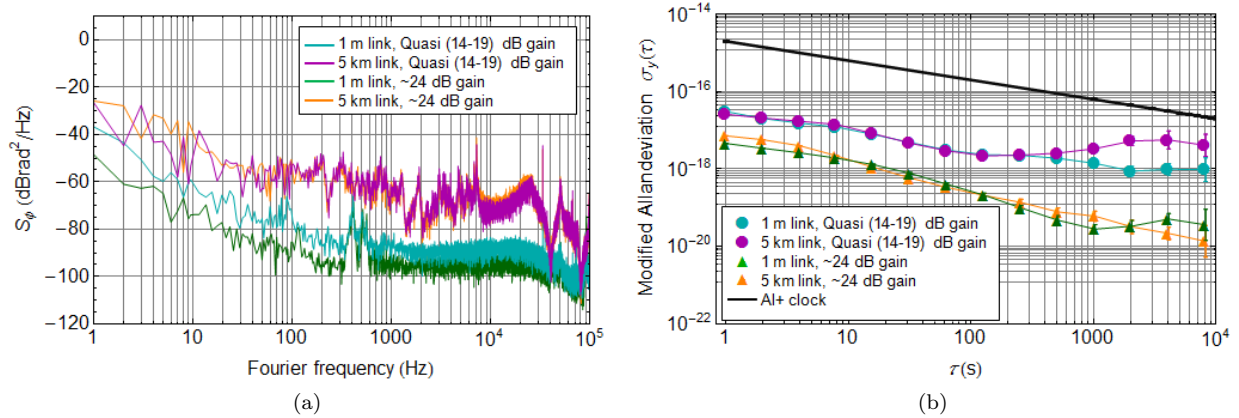


Figure 5.17: (a) Phase noise PSD spectra and (b) the MDEV of the noise compensated prototype 5 km and 1 m fiber link with optical amplification in a bidirectional and quasi-bidirectional arrangement. The black line in (b) represents the fractional frequency instability for a comparison between two Al^+ clocks [1]. All measurements are performed with the wooden box.

Chapter 6

Conclusion & Outlook

A laboratory test setup is built to transfer an ultrastable optical frequency through a 5 km long optical fiber link. The noise added to the frequency of the signal due to temperature fluctuations and acoustic noise in the fiber link is measured by sending part of the light back through the link. The round-trip light is used to create a beat note with light coming directly from the laser using a MMI. The beat note is subsequently phase locked to a rubidium clock using a PID-controller and a VCO acting on an AOM, and the noise is compensated by changing the frequency (and thereby the phase) of the light with the AOM. Due to temperature fluctuations and acoustic noise in the laboratory, the uncompensated fibers (out-of-loop paths) add noise to the local and remote signal. It is shown that this may be mitigated by placing the whole setup, apart from the 5 km fiber link, under a wooden box lined with acoustically damping material.

The performance of the phase noise compensated fiber link is characterized (in terms of the phase noise PSD and Allan deviation) at the remote end of the fiber link, where the remote signal is compared with the light coming directly from the laser. The phase noise spectra show interferometric noise at Fourier frequencies of < 50 Hz and delay-unsuppressed noise at $50 - 3000$ Hz, in accordance with the model and observations given by Williams *et. al.* [2]. The MDEV of the compensated 5 km link gives a relative frequency instability of 1×10^{-18} at 1 s, reaching 4×10^{-20} after 1×10^3 s. The relative frequency instability with the wooden box installed at 1 s averaging time is two orders of magnitude smaller than without the wooden box. A frequency drift is observed on a time scale of $10^3 - 10^4$ s, which may be caused by small residual temperature fluctuations inside the box. This drift causes the fractional frequency instability to rise up to 2×10^{-19} after 8×10^3 s. The out-of-loop paths should be shortened to obtain results with fractional frequency instabilities $< 10^{-20}$ [2].

In this project, the use of SOAs (as opposed to commonly used EDFAs) to compensate fiber attenuation in long fiber links is investigated for the first time. SOAs are tested in a bidirectional and quasi-bidirectional configurations. These optical amplifiers have a broad gain wavelength range and can be used to amplify wavelengths outside the C-band used in commercial networks, which allows bypassing EDFAs (which are typically unidirectional) with custom bidirectional amplifiers, and which avoids having to sacrifice C-band telecommunication bandwidth. The bidirectional configuration adds frequency instability, but the increase remains less than one order of magnitude over the full range of averaging times. The quasi-bidirectional configuration gives a relative frequency instability of 3×10^{-17} at 1 s, reaching 4×10^{-18} at 8×10^3 s, and is limited by 6 m of uncompensated fiber in the quasi-bidirectional amplifier.

All results are compared with the fractional frequency instability of a comparison between two high-accuracy optical Al^+ clocks [1]. The MDEV of the comparison between the clocks gives an instability of $2.0 \times 10^{-15} \tau^{-1/2}$. The fractional frequency instability of the uncompensated link is more than the instability of the Al^+ clocks and is therefore not capable of transferring the accurate time and frequency of the Al^+ clocks without adding a significant amount of noise. The fractional frequency instability of the compensated 5 km link is 2-3 orders of magnitude less than the instability of the Al^+ clock on a time scale of $1-8 \times 10^3$ s for the unamplified and bidirectional amplified links. Even in the case of the quasi-bidirectional amplification, the link stability remains below the Al^+ clock stability. Therefore, the active noise compensated 5 km link will not add a significant amount of noise to the frequency comparison of high-accuracy optical Al^+ clocks (at least at time scales 10^4-10^5 s).

The demonstration of a noise-compensated fiber link using bidirectional SOAs offers potential advantages over existing methods that make use of EDFAs. For example, the use of out-of-band wavelengths may facilitate time and frequency transfer in existing optical telecommunications infrastructure without having to sacrifice valuable telecommunication bandwidth. The accuracy of such time and frequency transfer has been demonstrated to be much higher than satellite methods (*e.g.* GPS). Conversely, a very accurately synchronized optical network may enable terrestrial navigation, similar to GPS, but via wireless transmitters connected to the optical network.

Chapter 7

Bibliography

- [1] C. W. Chou, D. B. Hume, J. C. J. Koelemeij, D. J. Wineland, and T. Rosenband, “Frequency Comparison of Two High-Accuracy Al^+ Optical Clocks,” *Physical Review Letters* **104**, 070802 (2010).
- [2] G. Grosche, O. Terra, K. Predehl, R. Holzwarth, B. Lipphardt, F. Vogt, U. Sterr, and H. Schnatz, “Optical frequency transfer via 146 km fiber link with 10^{-19} relative accuracy,” *Optics Letters* **34**, 2270 (2009).
- [3] O. Lopez, A. Kanj, P. Pottie, D. Rovera, J. Achkar, C. Chardonnet, A. Amy-Klein, and G. Santarelli, “Simultaneous remote transfer of accurate timing and optical frequency over a public fiber network,” *Applied Physics B* **110**, 3 (2013).
- [4] K. Predehl, G. Grosche, S. M. F. Raupach, S. Droste, O. Terra, J. Alnis, Th. Legero, T. W. Hänsch, Th. Udem, R. Holzwarth, and H. Schnatz, “A 920-kilometer Optical Fiber Link for Frequency Metrology at the 19th Decimal Place,” *Science* **336**, 441 (2012).
- [5] P. A. Williams, W. C. Swann, and N. R. Newbury, “High-stability transfer of an optical frequency over long fiber-optic links,” *Journal of the Optical Society of America B* **25**, 1284 (2008).
- [6] G. B. Hocker, “Fiber-optic sensing of pressure and temperature,” *Applied Optics* **18**, 1445 (1979).
- [7] W. J. Riley, “Handbook of Frequency Stability Analysis,” NIST Special Publication 1065 (NIST, Boulder, CO, 2008).
- [8] L.-S. Ma, P. Jungner, J. Ye, and J. L. Hall, “Delivering the same optical frequency at two places: accurate cancellation of phase noise introduced by an optical fiber or other time-varying path,” *Optics Letters* **19**, 1777 (1994).
- [9] E. Hecht, *Optics* (Addison Wesley, 2002), 4th ed.
- [10] H. W. Schrage, J. J. van Daal and J. Stroeken, *Regeltechniek voor HTO* (HB Uitgevers, 2011), 4th ed.
- [11] E. A. Donley, T. P. Heavner, F. Levi, M. O. Tataw, and S. R. Jefferts, “Double-pass acousto-optic modulator system,” *Review of Scientific Instruments* **76**, 063112 (2005).
- [12] U. Tietze and C. Schenk, *Electronic Circuits- Handbook for Design and Applications* (Springer, 2008), 2nd ed.
- [13] S. T. Dawkins, J. J. McFerran, and A. N. Luiten, “Considerations on the Measurement of the Stability of Oscillators with Frequency Counters,” *IEEE Transactions on Ultrasonics, Ferroelectrics and Frequency Control* **54**, 918 (2007).
- [14] S. Kasap, *Optoelectronics and Photonics, Principles and Practices* (Pearson Education, 2001), 1st ed.

Chapter 8

Dankwoord

De vier maanden dat dit project duurde zijn voorbij gevlogen voor ik het doorhad. Dat deze maanden zo vlot zijn verlopen, heb ik te danken aan meerdere personen. Allereerst wil ik mijn begeleider Jeroen Koelemeij bedanken voor zijn enthousiasme, kunde en gedrevenheid. De samenwerking verliep altijd goed, doch enigszins uit fase. Waar hij als echte nachtbraker nog een mail in de late uren stuurde, werkte ik in de vroege ochtend weer verder met de nieuwe inzichten/opmerkingen. Samen met de bijna dagelijkse besprekingen vormde dit een soort begeleiding waar ik mij goed in kon vinden. Ik heb tijdens deze periode ook veel geleerd van het programma 'Mathematica' door Jeroens verhelderende voorbeeldprogramma's die altijd met de variabele genaamd 'aap' begonnen.

Tjeerd Pinkert wil ik bedanken voor zijn dagelijkse begeleiding tijdens dit project. Hij was dé persoon waarbij ik aan kon kloppen wanneer mijn signaal weer eens ver te zoeken was of wanneer de laser uit lock was gegaan. Aangezien Tjeerd elektrotechniek heeft gestudeerd, heb ik ook veel kunnen leren van het vak dat mij soms nog enige zorgen baart. Kjeld Eikema wil ik bedanken voor het gebruik van de ultrastabiele Hz laser. Zonder deze laser was dit project niet van de grond gekomen. Rob Kortekaas wil ik bedanken voor de technische ondersteuning van dit project.

Al met al heb ik dit afstudeerproject als een zeer leerzame en leuke tijd ervaren.

Appendix A

List of components

Amount	Laser system	Brand	Type
1	Ultrastable CW laser (sub Hz linewidth)	Menlo systems	-
Amount	Free space Optics	Brand	Type
1	Polarization beam splitter	Thorlabs	PBS104
2	Plano-convex lens $f=75$ mm	Thorlabs	LA1608-C
2	Plano-concave lens $f=-50$ mm	Thorlabs	LA1715-C
2	Plano-convex lens $f=150$ mm	Thorlabs	LA1433-C
2	Acousto-Optic Modulator	Brimrose	IPF-150-100-1500
5	Mirrors	Thorlabs	BB1-E04-10
Amount	Fiber Optics	Brand	Type
1	5 km SMF-28 PM Link	-	-
2	(95-5)% beamsplitter SMF-28 non PM Single-Mode	-	-
1	(5-50)% beamsplitter SMF-28 non PM Single-Mode	-	-
1	Faraday mirror	General Photonics	NFRM-15-FC/APC
4	Collimation lens	Thorlabs	F240APC - 1550
2	Polarization controller SMF-28 PM Single-Mode	PolaRite	-
1	Eigenlight SMF-28 PM Single-Mode	PolaRite	-
2	Semi-conductor optical amplifier	-	-
Amount	Elektronics	Brand	Type
1	VCO	-	-
2	DDS	VU Electronics department	-
1	Lockbox	VU Electronics department	-
Amount	Equipment for the measurements	Brand	Type
1	Frequency counter	Agilent	53230A
1	Spectrum analyser	Agilent	E440A
1	10 MHz Clock	Stanford Research Systems	PRS10

Table A.1: List of used components

Appendix B

Acousto-optic modulators

An acousto-optic modulator (AOM) consists of a piezoelectric crystal with two electrodes attached to the surface [14]. One electrode acts as a transducer, whereas the other electrode acts as an absorber, so that application of a time-varying voltage to the electrode causes ultrasonic sound waves with frequency Λ that travel through the crystal. These acoustic waves lead to a periodic variation in the refractive index, n , of the crystal and thereby create a diffraction grating. The angle of diffraction, θ , depends on Λ , the wavelength of the light, λ , and n ; this is called the Bragg condition:

$$\sin \theta = \frac{\lambda}{\Lambda n} \quad (\text{B.1})$$

This diffraction can be seen as a photon-phonon scattering where the optical field is described by photons and the acoustic field by phonons. The total energy and momentum of the system must be conserved. From this it follows that the incoming angular frequency of the photon ω_i is shifted by an amount Ω , the angular frequency of the phonon, resulting in an outgoing photon with frequency ω_d . Likewise, the wave vector k_i of the photon is shifted to a new value k_d , because of the wave vector κ of the phonon. Equations B.2 and B.3 describe these two conditions [11].

$$\omega_d = \omega_i \pm \Omega \quad (\text{B.2})$$

$$k_d = k_i \pm \kappa \quad (\text{B.3})$$

Note that the wave vectors are actually three-dimensional vectors. In principle, this process can also take place at higher order, in which case a photon scatters off multiple phonons, thereby acquiring a frequency shift of several Ω . Figure B.1 shows the first order diffraction of the AOM, which can produce a positive as well as a negative shift to the frequency of the light.

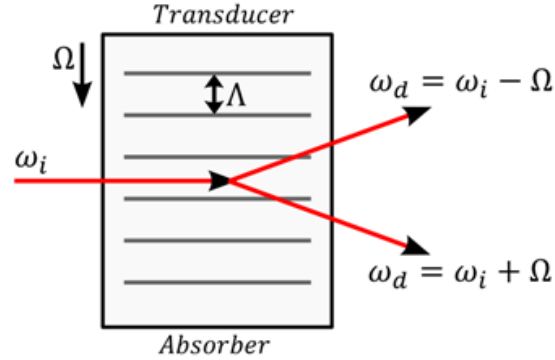


Figure B.1: Schematic of an acousto-optic modulator (AOM). The light beam may be diffracted into several orders, but only the first order of diffraction is depicted in this figure.

B.1 Polarization dependence of the AOM

During a round trip, the optical signal passes through each AOM twice. However, the polarization state is rotated by $\pi/2$ at the FM. It is therefore necessary to know the dependence of the AOM diffraction efficiency on polarization. In particular, the double-pass efficiency of the AOM should not be too low. Below, a measurement of the relative diffraction efficiencies η_x and η_y is presented. A half wave plate is used to test the dependence of the efficiency of the AOM on the polarization of the light, depicted in figure B.2. The polarization of the light is changed by rotating the half wave plate. The original polarization of the beam is linear and horizontal.

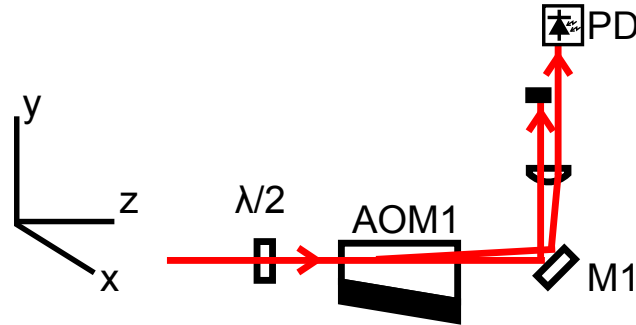


Figure B.2: Setup for determining the dependence of AOM diffraction efficiency on polarization angle.

The amount of light that is diffracted into the first order by the AOM (P) is measured as a function of the angle of the half wave plate ($\alpha_{\lambda/2}$). The results of this measurement are shown in figure B.3. The results can be fitted with a sinusoidal fit function in order to obtain the efficiency of the AOM in the x and y direction, η_x and η_y , respectively. The electric field E of the light can be decomposed into two components, E_x and E_y ,

$$E_x = E\eta_x \cos(\theta) \quad (\text{B.4})$$

$$E_y = E\eta_y \sin(\theta) \quad (\text{B.5})$$

The intensity (and therefore the measured power) of the light is proportional to E^2 ,

$$I \sim E^2 = \left[\sqrt{E_x^2 + E_y^2} \right]^2 = E^2 [\eta_x^2 \cos^2(\theta) + \eta_y^2 \sin^2(\theta)] \quad (\text{B.6})$$

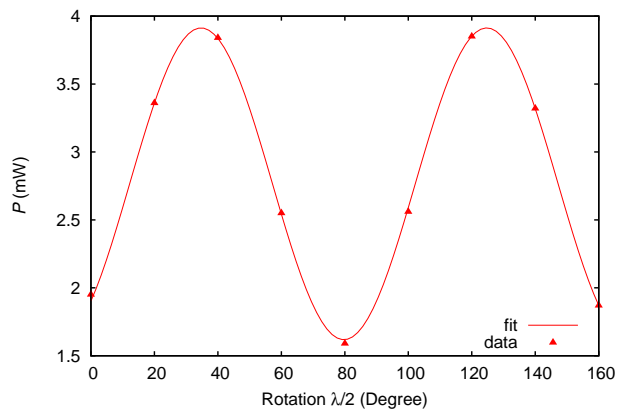


Figure B.3: Polarization dependence of the AOM.

The efficiencies listed in table B.1 are the results of the fit with equation B.6 (figure B.3). Note that the absolute values of the efficiencies are not only dependent on the polarization of the beam, properties of the beam (diameter, wavefront curvature) inside the AOM.

From table B.1 it is clear that horizontal-to-vertical diffraction efficiency ratio is about 2.4, which is acceptable.

Parameter	Value	Standard error
η_x	0.318	0.001
η_y	0.4945	0.0009

Table B.1: The efficiency of the AOM in the x - and y -direction.

Appendix C

Gaussian beam waist measurements

The laser beam diameter was measured in order to determine the minimal waist of the beam inside the AOMs. To measure the beam profile, the beam is partially blocked by a knife-edge while the remaining power of the beam is measured with a power meter. Figure C.1 shows the knife-edge and the x, y, z directions.

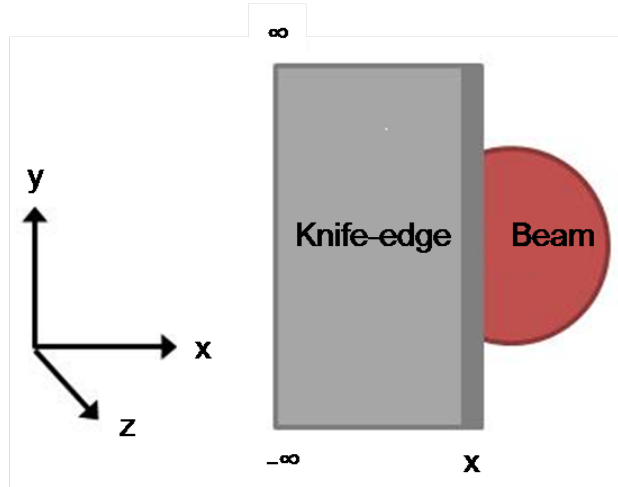


Figure C.1: Measuring the beam diameter of the laser light.

For a Gaussian beam, the measured power as a function of the position of the knife-edge can be described as

$$P(x) = \frac{P_0}{2} \left[1 + \operatorname{erf} \left(\frac{\sqrt{2}(x)}{w} \right) \right] \quad (\text{C.1})$$

where $P(x)$ is the power measured at a certain position (x) of the knife edge and P_0 is the measured power when the beam is fully unblocked. The remaining power could be measured for several positions of the knife edge in the x -axis so that the results can be fitted according to this equation. However, it suffices to measure the power only for two positions of the knife edge to determine the beam diameter. The measured power at $x = w/2$ and $x = -w/2$ is

$$P(w/2) = \frac{P_0}{2} \left[1 + \operatorname{erf} \left(\frac{\sqrt{2}(w/2)}{w} \right) \right] \approx 0.841P_0,$$

$$P(-w/2) = \frac{P_0}{2} \left[1 + \operatorname{erf} \left(\frac{\sqrt{2}(-w/2)}{w} \right) \right] \approx 0.159P_0, \text{ respectively.}$$

Thus, the knife edge can be positioned at the position where the power of the beam is only $0.841P_0$. After writing down the position x_1 using a micrometer screw, this procedure can be repeated for $0.159P_0$, which

results in a second value x_2 . The waist, $w(z)$, of the beam at a certain z -position is then calculated as $|x_1 - x_2|$. The beam radius as function of the z -position of the knife edge is given by equation C.2

$$w(z) = w_0 \sqrt{1 + \left(\frac{\lambda z}{\pi w_0^2} \right)^2} \quad (\text{C.2})$$

where w_0 is the minimal beam radius and z_0 is the z -position of w_0 . z_0 and w_0 may be determined with the help of equation C.2 by measuring the size of the waist at two different positions, provided it is known whether z_0 is located in front of, in between, or behind the two positions z_1 and z_2 .

Appendix D

Test of the Allan deviation code

The computer codes that are written for the overlapping and modified Allan deviation are tested by comparing the results of a test dataset of NIST [7] with the results of the written code. The code is tested with a 1000-point dataset. This dataset is generated with the recurrence relation

$$n_{i+1} = \text{Mod}[16807n_0, 2147483647] \text{ with } n_0 = 1234567890. \quad (\text{D.1})$$

The results are listed in table D.1.

Function	NIST	Code in mathematica
Maximum	9.957453×10^{-1}	9.957453×10^{-1}
Minimum	1.371760×10^{-3}	1.371760×10^{-3}
Average	4.897745×10^{-1}	4.897745×10^{-1}
Standard deviation (1)	2.884664×10^{-1}	2.884664×10^{-1}
Normal Allan Deviation (1)	2.922319×10^{-1}	2.922319×10^{-1}
Normal Allan Deviation (10)	9.965736×10^{-2}	9.965736×10^{-2}
Normal Allan Deviation (100)	3.897804×10^{-2}	3.897804×10^{-2}
Overlapping Allan Deviation (1)	2.922319×10^{-1}	2.922319×10^{-1}
Overlapping Allan Deviation (10)	9.159953×10^{-2}	9.159953×10^{-2}
Overlapping Allan Deviation (100)	3.241343×10^{-2}	3.241343×10^{-2}
Modified Allan Deviation (1)	2.922319×10^{-1}	2.922319×10^{-1}
Modified Allan Deviation (10)	6.172376×10^{-2}	6.172376×10^{-2}
Modified Allan Deviation (100)	2.170921×10^{-2}	2.170921×10^{-2}

Table D.1: Test results from the dataset that was generated with equation D.1

The code is written in Mathematica 8.0.4. Figure D.1 contains a screenshot of the code for the overlapping (ODEV) and modified (MDEV) Allan deviation calculations. This figure also shows the code that is used to test the calculations. The ODEV and MDEV calculations are integrated in a more complex program that is able to save and plot the data.

```

fx = (RecurrenceTable[{a[x + 1] == Mod[16807 * a[x], 2147483647], a[1] == 1234567890}, a, {x, 1, 1000}]) / 2147483647;
(*fx is the name of table of the 1000 testpoints*)
Nr = Length[fx]; (*The length of the data set*)
Nd = Nr + 1; (*Nd=N in the report, amount of phase data*)
r0 = 1;
som = 0;
phase = Table[(*The frequency data is converted to phase data*)
  If[[] == 1, som = 0,
    int = fx[[] - 1]] * r0;
  som = som + int]
  , {[], 1, Nr}
];

AdevOverlappedPhase = Table[{2^j},
  m = 2^j; (*The averaging factor*)
  r = m * r0; (*Sampling interval*)
  Sqrt[1 / (2 * (Nd - 2 * m) * r^2) * Total[Table[(phase[[i + m]] - 2 * phase[[i + m]] + phase[[i]]]^2, {i, 1, Nd - 2 * m}]]] * 1.], (*ODEV*)
  {[], 0, rmax - 1}];

AdevModPhase = Table[{2^j},
  m = 2^j; (*The averaging factor*)
  r = m * r0; (*Sampling interval*)
  Sqrt[1 / (2 * m^2 * r^2 * (Nd - 3 * m + 1)) * ParallelSum[Total[Table[(phase[[i + 2 * m]] - 2 * phase[[i + m]] + phase[[i]]]^2, {i, j, j + m - 1}]]^2, {j, 1, Nd - 3 * m + 1}] * 1.], (*MDEV*)
  {[], 0, rmax}];

```

Figure D.1: The mathematica code that is used for calculating the ODEV and MDEV.

The code that is written for the overlapping Allan deviation and the modified Allan deviation use the functions `Table` and `Total` to sum up elements of the phase data. Mathematica also contains a function called `Sum` which might be the first function to use in this case. However the `Sum` function requires more time to evaluate than first forming a `Table` and then using `Total` to calculate the sum of the table, as shown in figure D.2 where a test table is used with 400 000 points. The same calculation is performed using either the functions `Table` and `Total` or the function `Sum`. It takes 1.014 seconds for the `Sum` function while it only takes 0.172 seconds for the `Table` and `Total` function to calculate the sum.

```
■ Test Data

In[3]:= test = Table[j, {j, 0, 400000}]; (*A table of 400000 datapoints*)

■ Timing the Sum function and comparing this with using the Total & Table function

In[4]:= Timing[Total[Table[test[[i + 1]] + test[[i + 2]], {i, 0, Length[test] - 2}]] (*Using Table and Total*)
Out[4]= {0.172, 160000000000}

In[5]:= Timing[Sum[test[[i + 1]] + test[[i + 2]], {i, 0, Length[test] - 2}]] (* Using Sum*)
Out[5]= {1.014, 160000000000}
```

Figure D.2: The `Sum` function is compared with a combination of the `Total` and `Table` function. The `Sum` function appears to be slower than the combination of the `Total` and `Table` function.

Appendix E

Characteristics of the used SOAs

The performance of the SOAs is characterized as a function of the bias current (I) that is applied to the SOAs. The power of the amplified light is measured with a fiber-pigtailed power meter. This power meter can also attenuate the light that passes through the meter. The power of the amplified light is measured with and without blocking the light of the laser. When the laser light is blocked, the measured power is the amplified spontaneous emission (ASE) of the SOA. The measurements can be found in the appendix, chapter E. The actual power of the signal can be calculated with equation 5.1.

$$P_{s, \text{SOA}}(I) = P_{\text{SOA}}(I) - P_{\text{ASE}}(I) \quad (\text{E.1})$$

where P_{SOA} is the total power while the laser is unblocked and P_{ASE} is the power measured when the laser is blocked. Since the power meter measures the power in dBm, equation 5.2 is used.

$$P_{s, \text{SOA}}(I) \text{ (dBm)} = 10 \times \log [10^{P_{\text{SOA}} \text{ (dBm)}/10} - 10^{P_{\text{ASE}} \text{ (dBm)}/10}] \quad (\text{E.2})$$

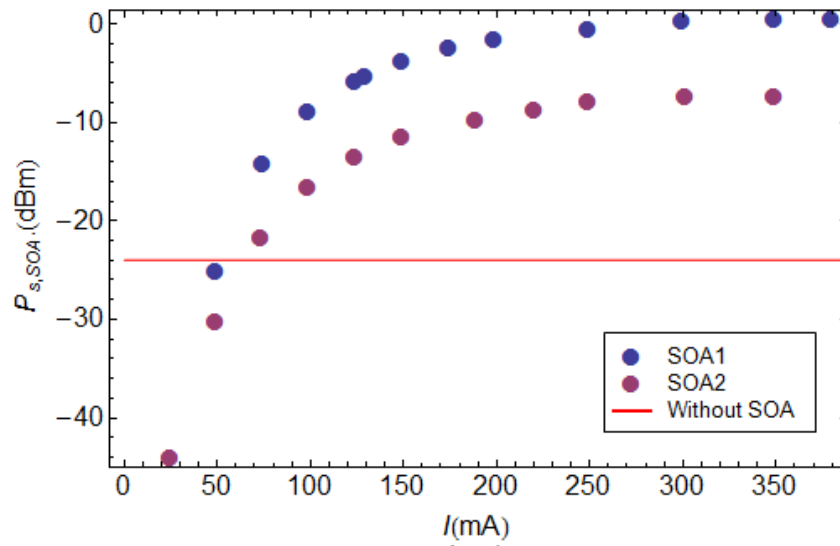
The results are shown in table E.1 and table E.2 for SOA1 and SOA1 respectively.

I (mA) ± 0.005 mA	P_{SOA} (dBm) ± 0.05 dBm	P_{ESA} (dBm) ± 0.05 dBm	$P_{s, \text{SOA}}$ (mW)	$P_{s, \text{SOA}}$ (dBm)
25.02	-30.3	-30.3	$0 \pm 2 \times 10^{-5}$	$-\infty$
50.07	-21.7	-24.3	0.0030 ± 0.0002	-25.2 ± 0.2
75.03	-13.3	-20.3	0.0374 ± 0.0007	-14.27 ± 0.08
100.02	-8.3	-17.2	0.129 ± 0.002	-8.90 ± 0.07
125.08	-5.3	-14.8	0.262 ± 0.004	-5.82 ± 0.07
130.28	-4.8	-14.4	0.294 ± 0.005	-5.30 ± 0.07
150.06	-3.3	-12.9	0.416 ± 0.006	-3.80 ± 0.07
175.21	-2.0	-11.4	0.559 ± 0.009	-2.53 ± 0.07
200.12	-1.1	-10.3	0.68 ± 0.02	-1.66 ± 0.07
250.09	0.1	-8.6	0.89 ± 0.02	-0.53 ± 0.07
300.44	0.9	-7.5	1.05 ± 0.02	0.22 ± 0.07
350.12	1.2	-7.0	1.12 ± 0.02	0.49 ± 0.07
380.45	1.2	-6.8	1.11 ± 0.02	0.45 ± 0.07
without SOA1	-24.0	$-\infty$	0.00398 ± 0.00005	-24.0 ± 0.05

Table E.1: The power of the light amplified by SOA1 that is used in the bidirectional and quasi-bidirectional setup.

I (mA) ± 0.05 mA	P_{SOA} (dBm) ± 0.05 dBm	P_{ESA} (dBm) ± 0.05 dBm	$P_{s, \text{SOA}}$ (mW)	$P_{s, \text{SOA}}$ (dBm)
25.6	-27.6	-27.7	0.000004 ± 0.00004	-44 ± 5
50.5	-20.6	-21.1	0.0009 ± 0.0002	-30.2 ± 0.9
74.8	-16.2	-17.6	0.0066 ± 0.0005	-21.8 ± 0.3
100.1	-12.9	-15.3	0.022 ± 0.001	-16.6 ± 0.2
125.0	-10.6	-13.7	0.044 ± 0.002	-13.5 ± 0.1
150.3	-9.0	-12.5	0.070 ± 0.003	-11.6 ± 0.1
189.8	-7.5	-11.3	0.104 ± 0.003	-9.8 ± 0.1
221.3	-6.6	-10.7	0.134 ± 0.004	-8.7 ± 0.1
250.5	-5.9	-10.3	0.164 ± 0.005	-7.9 ± 0.1
302.2	-5.5	-10.0	0.182 ± 0.005	-7.4 ± 0.1
350.3	-5.5	-10.1	0.184 ± 0.005	-7.3 ± 0.1
without SOA2	-24.0	$-\infty$	0.00398 ± 0.00005	-24.0

Table E.2: The power of the light amplified by SOA2 that is used in the quasi-bidirectional setup.

Figure E.1: The output power of the signal ($P_{s, \text{SOA}}$) as a function of the current (I) through the SOAs. The red line depicts the signal power (P_s) when there is no SOA inserted.

Appendix F

Originele opdrachtomschrijving (Dutch)

Omschrijving afstudeerproject Chantal van Tour (De Haagse Hogeschool te Delft)

Periode

04/02/2013 31/05/2013

Begeleider

Dr. Jeroen Koelemeij, Vrije Universiteit Amsterdam

Wetenschappelijke context

In het LaserLaB VU is onlangs het project SuperGPS door optische netwerken van start gegaan. Het doel van dit project is de nauwkeurige tijd en frequentie van een atoomklok via het glasvezelnetwerk voor telecommunicatie te verspreiden naar gebruikers. Tijd en frequentie zullen hiervoor worden versleuteld in optische signalen, geproduceerd door lasers. Een dergelijk systeem kan in de toekomst niet alleen extreem nauwkeurige netwerk-synchronisatie mogelijk maken, maar kan ook als basis dienen voor nieuwe plaatsbepalingssystemen die een veel hogere nauwkeurigheid en beter bereik hebben dan het huidige GPS. Ook kunnen met deze technologie optische klokken op grote afstand met elkaar worden vergeleken, wat van belang is voor fundamenteel natuurkundig onderzoek in Nederland en Europa.

Omschrijving afstudeerproject

Het doel van het afstudeerproject is het bouwen en karakteriseren van een zogeheten gecompenseerde en optisch versterkte glasvezelverbinding. Deze glasvezelverbinding zal worden gebruikt om het licht van een ultrastabiele laser in LaserLaB (lijnbreedte <1 Hz) over een grote afstand (100–300 km) te transporteren. De verzwakking die het licht in de glasvezel ondergaat zal worden gecompenseerd door een optische versterker. Trillingen en thermische uitzetting van de glasvezel hebben echter een negatieve uitwerking op de lijnbreedte van de laser. Door een deel van het licht na transport weer terug de glasvezel in te sturen, pikt de optische fase van het licht twee keer dezelfde verstoring op. Deze verstoring kan bij het beginpunt van de glasvezel worden gedetecteerd met behulp van een Michelson-Morley interferometer (MMI). Via terugkoppeling op de laser via een phase-locked loop (PLL) kan de verstoring door de glasvezel worden gecompenseerd, zodanig dat de getransporteerde laser zijn <1 Hz lijnbreedte behoudt. Het experimentele werk voor de projectopdracht bestaat dus uit:

- Het opstellen van een test-glasvezelverbinding bestaande uit een telecomlaser, een glasvezelspoel, een optische fasemodulator (in dit geval een acousto-optische modulator, AOM), en een bidirectionele optische versterker (een halfgeleider optische versterker) [3 weken];
- Het opbouwen en inregelen van de MMI en PLL voor actieve compensatie van de fluctuaties in de optische padlengte van de glasvezel [5 weken];

- Het karakteriseren van de stabiliteit en ruis eigenschappen van het compensatiecircuit en de getransporteerde laser (Allan deviation en phase noise power spectral density analyse), onder verschillende omstandigheden [4-6 weken].

Als het project slaagt, zal de technologie worden ingezet op zowel korte glasvezelverbindingen tussen verschillende labs binnen het LaserLaB als lange verbindingen (bijvoorbeeld de 317 km lange SURFnet-verbinding tussen VU en KVI Groningen). Ook kan het leiden tot een co-auteurschap van het eerste wetenschappelijke artikel waarin de technologie wordt beschreven.